



Supplementary Materials for

**Phospho-dependent phase separation of FMRP and CAPRIN1 recapitulates
regulation of translation and deadenylation**

Tae Hun Kim, Brian Tsang, Robert M. Vernon, Nahum Sonenberg, Lewis E. Kay,
Julie D. Forman-Kay*

*Corresponding author. Email: forman@sickkids.ca

Published 23 August 2019, *Science* **365**, 825 (2019)
DOI: 10.1126/science.aax4240

This PDF file includes:

Materials and Methods
Supplementary Text
Figs. S1 to S20
Caption for movie S1
References

Other supplementary material for this manuscript includes the following:

Table S1 (Excel format)
Movie S1

Materials and Methods

Protein Expression and Purification

FMRP (445-632)

The low-complexity disordered region of human FMRP (445-632) was expressed and purified as previously described (18). Briefly, His-SUMO-FMRP was transformed into *Escherichia coli* (*E. coli*) BL21-CodonPlus(DE3) RIL cells and grown at 37 °C in LB. Protein expression was induced with 0.5 mM IPTG at an OD_{600nm} ~0.6 and grown overnight at 25 °C. Cells were harvested and pelleted via centrifugation. Pellets were stored at -20 °C or used immediately.

Cells were lysed in buffer containing 6 M guanidine hydrochloride (GdnHCl), 50 mM Tris pH 8, 500 mM NaCl, 20 mM imidazole and 2 mM β -mercaptoethanol (β ME) and sonicated for 4.5 mins (2s on, 1 s off). Lysed cells were spun down and filtered through a 1 micron filter. The lysate was then loaded onto Ni-NTA resin (GE Healthcare) equilibrated with lysis buffer. The Ni-NTA resin was washed with 10 column volumes of lysis buffer followed by 5 column volumes of lysis buffer without 6 M GdnHCl. Elution buffer containing 50 mM Tris pH 8, 500 mM NaCl, 300 mM imidazole, 2 mM β ME was used to elute His-SUMO-FMRP. The His-SUMO tag was cleaved with ULP1 protease while dialyzed against cleavage buffer containing 50 mM Tris pH 8, 150 mM NaCl, 20 mM imidazole, 2mM β ME overnight. FMRP was separated from the His-SUMO tag by loading the protein onto Ni-NTA resin and collecting the flow-through. SDS-PAGE gel was used to confirm successful cleavage of the His-SUMO tag and separation of the tag from FMRP. The flow-through was concentrated and further purified using a Superdex 75 column (GE Healthcare) equilibrated with buffer containing 4 M GdnHCl, 50 mM Tris pH 8, 500 mM NaCl, 2 mM β ME. FMRP containing fractions were pooled together. The purity of FMRP was confirmed with SDS-PAGE gel and intact mass spectrometry.

CAPRIN1 (607-709)

The low-complexity disordered region of human CAPRIN1 (607-709) was subcloned into a pET-His-SUMO vector and transformed into *E. coli* BL21-CodonPlus(DE3) RIL. Protein expression and cell harvesting were performed in the same way as His-SUMO-FMRP. For ¹³C, ¹⁵N labelled sample preparation, minimal media (6 g of NaHPO₄, 3 g of KH₂PO₄, 0.5 g of NaCl, 1 g of ¹⁵NH₄Cl, 3 g of [U-¹³C]-glucose, 2 mM MgSO₄, 50 ug/ml of kanamycin, 10 mg of biotin and thiamine in 1 L at pH 7.4) was used. Harvested cell pellets were stored at -20 °C or used immediately. Cells were lysed with cold lysis buffer containing 6 M GdnHCl, 50 mM Tris pH 8, 500 mM NaCl, 20 mM imidazole and 2 mM β ME. The lysed cells were spun down and the lysate loaded onto Ni-NTA resin (GE Healthcare) equilibrated with lysis buffer. The Ni-NTA resin was washed with 10 column volumes of lysis buffer followed by 5 column volumes of lysis buffer without 6M GuHCl. Elution buffer containing 50 mM Tris pH 8, 500 mM NaCl, 300 mM imidazole and 2 mM β ME was used to elute His-SUMO-CAPRIN1. The His-SUMO tag was cleaved with ULP1 protease while dialyzed against cleavage buffer containing 50 mM Tris pH 8, 150 mM NaCl, 20 mM imidazole and 2mM β ME overnight. CAPRIN1 was separated from the His-SUMO tag by loading the cleaved protein onto Ni-NTA resin and the flow-through was collected. SDS-PAGE gel was used to confirm the cleaved and separated CAPRIN1 product from the His-SUMO tag. The flow-through was concentrated and further purified using a Superdex 75 column (GE Healthcare) equilibrated with 4 M GdnHCl, 50 mM Tris pH 8, 500

mM NaCl and 2 mM β ME). CAPRIN1 containing fractions were pooled together. The purity of CAPRIN1 was confirmed with SDS-PAGE gel and intact mass spectrometry.

CNOT7

The gene for human CNOT7 deadenylase (1-285) was synthesized (ThermoFisher) and subcloned into a pET-SUMO vector. Cells were grown to OD_{600nm} of 0.6 and induced with 0.25 mM IPTG at 20 °C in LB medium containing 50 ug/ml of kanamycin and grown overnight. Cells were harvested and stored at -20 °C. Pellets were lysed in ice-cold lysis buffer (20 mM Tris-HCl pH 7.6, 500 mM NaCl, 10 mM MgCl₂, 10% glycerol, 10 mM imidazole, 2 mM β ME supplemented with a EDTA-free Roche protease inhibitor and DNase1) using a Q Sonica Q500 (30% amplitude, 2 seconds on/ 2 seconds off, 5 minutes). After spinning down, the lysate was loaded to pre-equilibrated Ni-NTA resin (GE Healthcare) and washed with 10 column volumes of wash buffer (lysis buffer with 20 mM imidazole) and eluted with 5 column volumes of elution buffer (lysis buffer with 300 mM imidazole). The eluted protein was treated with ULP1 protease to cleave off the His-SUMO tag and dialyzed against buffer containing 50 mM Tris pH 8, 150 mM NaCl, 20 mM imidazole, 10 mM MgCl₂, 2 mM β ME and 10% glycerol overnight. After dialysis, the protein was loaded onto Ni-NTA resin to separate the His-SUMO tag from CNOT7. The flow-through was concentrated and applied to a Superdex 75 column (GE-Healthcare) equilibrated in 50 mM Tris pH 8, 200 mM NaCl, 10 mM MgCl₂, 5% glycerol and 2mM β ME at 4 °C. CNOT7 fractions were collected and purity was confirmed with SDS-PAGE gel and intact mass spectrometry.

eIF4E

The human eIF4E was subcloned into a pET-His-SUMO vector and transformed into *E. coli* BL21-CodonPlus(DE3) RIL. Cells were grown to OD_{600nm} of 0.6 and induced with 0.5 mM IPTG at 16 °C in LB medium containing 50 ug/ml of kanamycin and grown overnight. Cells were harvested with ice-cold lysis buffer containing 20 mM NaPO₄ pH 7.6, 500 mM NaCl, 20 mM imidazole, 2 mM β ME, EDTA-free Roche protease inhibitor and lysed using Q Sonica Q500 (30% amplitude, 2 seconds on/ 2 seconds off, 5 minutes). Lysed cells were spun down and the resulting lysate was loaded onto Ni-NTA resin (GE Healthcare) equilibrated with lysis buffer. The Ni-NTA resin was washed with 10 column volumes of lysis buffer. Elution buffer containing 20 mM NaPO₄ pH 7.6, 500 mM NaCl, 400 mM imidazole, and 2 mM β ME was used to elute His-SUMO-eIF4E. The His-SUMO tag was cleaved with ULP1 protease while dialyzed against cleavage buffer containing 50 mM Tris pH 7.4, 150 mM NaCl, 2mM β ME overnight. eIF4E was separated from His-SUMO tag by loading the cleaved protein onto Ni-NTA resin and the flow-through was collected. SDS-PAGE gel was used to confirm the cleaved and separated eIF4E product from the His-SUMO tag. The flow-through was concentrated and further purified using a Superdex 75 column (GE-Healthcare) equilibrated with buffer containing 50 mM NaPO₄ pH 7.4, 200 mM NaCl, 2 mM DTT, 1 mM EDTA, 2 mM, Benzamidine-HCl. eIF4E containing fractions were pooled together. The purity of eIF4E was confirmed with SDS-PAGE gel and intact mass spectrometry.

RNA Preparation

RNA including sc1, FITC-sc1, FITC-polyA were purchased from Sigma-Aldrich as lyophilized samples. 100 μ M stocks were reconstituted in water and stored in -20 °C. Working stocks were diluted into specific assay buffers.

Protein Phosphorylation Reactions

FMRP was phosphorylated using Casein kinase II (CK2, NEB), while CAPRIN1 was phosphorylated using the kinase domain of mouse Eph4A (587-896) (31) with SUMO attached at the N-terminus. Both phosphorylation reactions followed the same dialysis method. Briefly, purified proteins were first concentrated to 100 μ M in a reaction buffer containing 25 mM Tris pH 7.4, 50 mM KCl, 10 mM MgCl₂ and 5 mM ATP and transferred to a 3 kDa cut-off dialysis tubing. 20 μ L of CK2 or SUMO-Eph4A was added to the corresponding protein and the reaction was dialysed against 4 L of the reaction buffer at room temperature or at 4 °C. Fresh dialysis was changed every one or two days until the desired phosphorylation state was achieved. The phosphorylation state was confirmed via intact mass spectrometry from 10 μ L aliquots. After the desired phosphorylation state was achieved, the reaction was quenched with the addition of 4 M GdnHCl. The sample was then concentrated and passed through a Superdex 75 column (GE-Healthcare) to re-purify each protein and subsequently stored in -20 °C or dialyzed into specific assay buffer. The final phosphorylation state was re-confirmed via intact mass spectrometry. LC-MS/MS was used to identify specific phosphorylated residues (fig. S3) which shows that CK2 phosphorylation is not random.

Different phosphorylated states of FMRP were used in various experiments. We used the low-pFMRP only in the FRET experiments. The med-pFMRP was used in FRET experiments and also in NMR experiments to form the condensed pFMRP phase. The high-pFMRP was used in all other experiments.

Fluorescence labelling of Protein

FMRP and CAPRIN1

A fluorescence dye was added via maleimide linkage to a single cysteine in FMRP or CAPRIN1. FMRP has a natural single cysteine at position C584, while an artificial cysteine was introduced into CAPRIN1 at the C-terminal end (C710) via site-directed mutagenesis. For labelling reactions, both proteins were in buffers containing 50 mM Tris pH 7.5, 100 mM NaCl and 4 M GdnHCl. The proteins were first passed through a Hi-Trap desalting column (GE-healthcare) to ensure that any residual reducing agents are removed. Then, protein samples were collected and immediately reacted with either 5x Cy3, Cy5, FITC (Lumioprobes) or Alexa488 (ThermoFisher) maleimide dye. The reaction was incubated overnight at 4 °C and quenched with excess DTT on the following day. Unreacted dye was removed with two steps. First, the protein was passed through a Hi-Trap desalting column equilibrated with 50 mM Tris pH 7.5, 100 mM NaCl, 4 M Gdn-HCl and 2mM DTT. De-salted samples were collected and passed through a Superdex 75 column (GE-Healthcare) equilibrated in the same buffer. Successful dye separation was confirmed by running the collected protein sample through SDS-PAGE gel and using a fluorescence reader to detect any remaining free dye. Labelling efficiency was determined via mass spectrometry analysis.

CNOT7 and eIF4E

A fluorescence dye was added via maleimide linkage to potentially six cysteines present in CNOT7 at amino acid positions 13, 18, 67, 148, 202 and 256. For labelling reactions, CNOT7 in sample buffer containing 50 mM HEPES, 150 mM NaCl, 10 % Glycerol, 2 mM DTT at pH 7.4 was passed through a Hi-Trap desalting column (GE-Healthcare) pre-equilibrated with the

sample buffer without DTT to ensure that any residual reducing agents are removed. CNOT7 was collected and immediately reacted with Cy5 mono-maleimide dye (Lumioprobe). Concentration of Cy5 mono-maleimide dye was around 20% of CNOT7 concentration in order to label a small fraction of solvent-exposed cysteines. The reaction was incubated at room temperature for 1 hour and immediately quenched with excess DTT. Unreacted dye was removed with two steps. First, CNOT7 was passed through a Hi-Trap desalting column (GE-Healthcare) equilibrated with buffer containing the sample buffer. De-salted samples were collected and passed through a Superdex 75 column (GE-Healthcare) equilibrated in the same sample buffer. Successful dye separation was confirmed by running the collected protein sample through SDS-PAGE gel and using a fluorescence reader to detect any remaining free dye. eIF4E was labelled with Alexa647 (ThermoFisher) in the same manner. Labelling efficiency was determined via mass spectrometry analysis.

Liquid Chromatography – Mass Spectrometry / Mass Spectrometry (LC-MS/MS)

All sample preparation was carried out at the SPARC Biocentre, Molecular Analysis division, The Hospital for Sick Children, Toronto. Samples were resuspended in 50 μ L of 50 mM NH_4HCO_3 , pH 8.3, and DTT was added to reduce cysteines at a final concentration of 10 mM. Cysteines were reduced at 60 °C for 1 hour. The sample was cooled to room temperature and iodoacetamide was added to a final volume of 20 mM. Samples (pFMRP or pYCAPRIN1) were incubated at room temperature in the dark for 30 minutes. Iodoacetamide was then inactivated by adding DTT to a final concentration of 40 mM. Protein samples were split into three, where MS grade TPCK-treated trypsin (Promega), Chymotrypsin, or Pepsin, was added to a final protease: protein ratio of 1:50-1:100. Samples were digested overnight at 37 °C. Samples were lyophilized, resuspended in 1 % TFA and the three digests were combined. Peptides were purified by homemade C18 tips, and then lyophilized again.

Samples were analyzed on a Thermo Scientific Orbitrap Fusion-Lumos Tribid Mass Spectrometer (ThermoFisher, San Jose, CA) outfitted with a nanospray source and EASY-nLC 1200 nano-LC system (ThermoFisher, San Jose, CA) and equipped with ETD mode. Lyophilized peptide mixtures were dissolved in 0.1 % formic acid and loaded onto a 75 μ m x 50 cm PepMax RSLC EASY-Spray column filled with 2 μ M C18 beads (ThermoFisher San, Jose CA) at a pressure of 900 Bar and a temperature of 60 °C. Peptides were eluted over 60 minutes at a rate of 250 nL/min using a gradient set up as follows, where Buffer A is 0.1% Formic acid and Buffer B is 80% Acetonitrile, 0.1% Formic Acid, all v/v in HPLC grade water.

Time	Duration	% B
0	0	3
17	17	25
49	32	44
51	2	100
60	9	100

Data were acquired using an FT-IT method. MS1 acquisition was performed with a scan range of 400m/z - 2000 m/z with a resolution set to 60 000, a maximum injection time of 120 ms and AGC target set to 4e5. Isolation for MS2 scans was performed in the quadrupole, with an isolation window of 1.6. MS2 scans were done in the linear ion trap with a maximum injection time of 35ms and an AGC target of 1e4. Ions were selected for CID fragmentation at 35%

normalized collision energy. Ions were also selected for an MS2 level scan in the Orbitrap with EtHCD. Herein, the resolution was set to 30000 and calibrated ETD dependant charge parameters were used. The dynamic exclusion was applied using a maximum exclusion list of 500 with one an exclusion duration of 10 s.

Isothermal Titration Calorimetry (ITC)

ITC binding experiments were performed using a MicroCal Auto-iTC200 (Malvern) in ITC buffer containing 25 mM NaPO₄ pH 7.4, and 5 mM β ME at 20 °C. Three experimental replicates were performed. Before the experiment, each protein sample was extensively dialyzed in ITC buffer three times. Proteins were passed through a 0.2 μ m filter and concentrations were determined using absorbance at 280 nm with calculated extinction coefficients. The ligand in the syringe contained either CAPRIN1, R-to-K-CAPRIN1 (all 15 arginines mutated to lysines), FMRP or pFMRP at 95 μ M. The cell contained FMRP, pFMRP or CNOT7 at 10 μ M or buffer. One experiment has 19 injections of 2 μ L each, injection duration of 4 seconds, injection interval of 180 seconds, stirring speed 750 RPM and reference power of 5 μ cal/sec. Origin 7.0 software was used to fit and calculate affinity constants (K_D), molar enthalpy (dH), and binding stoichiometries (N) using a single-site binding model. Interaction between CAPRIN1 and CNOT7 was fitted using a two-site binding model.

Fluorescence Resonance Energy Transfer (FRET) Assay

FRET experiments were performed using a SpectraMax i3x Multi-Mode Assay Plate Reader (Molecular Devices). A full fluorescence spectrum was collected from 555 nm to 800 nm, with an excitation at 535 nm. Three experimental replicates each with three technical replicates were performed. Each experiment consisted of 20 μ L reactions applied to a 384-well black bottom plate (Corning 3820). 10 μ M of pFMRP-Cy3 (donor) was mixed with a range of CAPRIN1-Cy5 (acceptor) concentrations in a buffer containing 25 mM NaPO₄ pH 7.4, and 2 mM DTT. Raw fluorescence values of the donor fluorescence (565 nm) were subtracted from the buffer background. FRET efficiency is calculated as the percent reduction (quenching) of the donor (pFMRP-Cy3) signal in the presence of increasing acceptor (CAPRIN1-Cy5) normalized to the highest value. Experimental data were fit to a Hill equation using GraphPad Software (Prism).

Microscopy Imaging of Condensate Samples

Phase separation between pFMRP or FMRP with CAPRIN1 and RNA was imaged on a confocal Leica DMI8 microscope equipped with a Hamamatsu C9100-13 EM-CCD camera with either a 40x or 60x objective. Cy3, Cy5 and FITC fluorescence were detected using a 561 nm (50 mW), 642 nm (50 mW), and 491 nm (50 mW) laser respectively. Higher resolution imaging was acquired with a Leica SP8 Lightning confocal microscope equipped with Leica hybrid detectors (HyD) using a 40X/1.3 (water) objective. Cy5 and FITC fluorescence were detected using a 638 nm (20 mW) and 488 nm (40 mW) laser, respectively. The images were deconvolved using the adaptive deconvolution algorithm provided in the Leica Lightning module. Samples were mixed to induce phase separation and immediately placed onto a 96 glass well plate (Eppendorf). Proteins and RNAs labelled with fluorophores (Cy3, Cy5, FITC, and Alexa488) were prepared in buffer containing 25 mM Na₂PO₄ pH 7.4 and 2 mM DTT. Two- or three-fold concentrated protein or RNA samples were prepared to account for the dilution in mixing with other components of the final samples. Note that molecular crowding reagents were not used. Images

represent droplets settled to the bottom of the plate. Images were analyzed using Volocity (Perkin Elmer) and ImageJ.

Sample Preparation of Protein Condensed Phase for NMR Spectroscopy

FMRP or pFMRP was dialyzed into a low salt NMR buffer containing 25 mM NaPO₄ pH 7.4, 10 mM TCEP and 10 % D₂O. Samples were concentrated using a 5 mL Amicon ultracentrifuge at room temperature to a low volume (~1 mL) and high concentration (~2 mM). Samples were left on ice to induce phase separation and then spun down using a microcentrifuge at 4 °C producing a bulk two phase system: protein depleted phase on top and protein condensed phase on the bottom. The concentration of each phase was measured via serial dilution into GdnHCl buffer and using A280 reading. ~200 µL of the protein condensed phase were transferred into a new microcentrifuge tube and thoroughly vortexed perturbing the phase and reforming a milky turbid solution. To that solution, 70 µL of highly concentrated (~6 mM) NMR active [¹³C, ¹⁵N]CAPRIN1 was added. The solution was incubated briefly on ice and then spun using a microcentrifuge. The final mixed sample was transferred to a 3-mm NMR tubes (Wilmad) for NMR experiments. A schematic diagram of sample preparation is shown in supplementary figure S7. See Supplementary text for more description of the difference between NMR samples of condensed phases of CAPRIN1 with either FMRP and pFMRP.

The relative concentrations of FMRP and CAPRIN1 or pFMRP and CAPRIN1 were evaluated using gel filtration chromatography. Condensed samples (FMRP-CAPRIN1 or pFMRP-CAPRIN1) and their corresponding dilute phases were passed through a Superdex 75 gel filtration column (GE-Healthcare). Peaks from elution profiles were integrated and compared to obtain relative protein concentrations. SDS-PAGE gels were used to confirm the purity of separated samples.

NMR Spectroscopy

NH-HSQC spectra of 100 µM [¹⁵N]CAPRIN1 with 0, 50, or 95 µM of pFMRP were recorded at 10 °C on a 600 MHz Varian spectrometer equipped with a cryogenic probe. NMR samples were in a buffer containing 25 mM NaPO₄, pH 7.4, 10 mM TCEP and 10% D₂O.

To obtain backbone resonance assignment of CAPRIN1 (607-709), a ¹³C, ¹⁵N labelled CAPRIN1 sample was prepared in a 25 mM MES, pH 5.5 buffer. HNCO, HN(CA)CO, HNCACB, CBCA(CO)NH, HNN, HACAN, and (HB)CBCA(CO)N(CA)HA spectra (32) were acquired at 25 °C on a 600 MHz Varian spectrometer equipped with a cryogenic probe. CON spectra (33) were acquired at 30 °C on an 800 MHz Bruker AVANCE-NEO spectrometer, equipped with a 5-mm TXO CryoProbe (¹³C optimized) with integrated cooled pre-amplifiers for ¹H, ¹³C, ¹⁵N, ²H channels equipped with an actively shielded single axis Z-gradient. The backbone resonance assignment of CAPRIN1 at pH 5.5 was transferred to the CON spectrum of CAPRIN1 in dilute phase at pH 7.4. Since there are no histidines in CAPRIN1 (607-709), transferring the resonance assignment from pH 5.5 to 7.4 did not require additional NMR experiments. Carbon-detected CBCANCO and CBCACON spectra (33, 34) acquired at pH 7.4 further validated the CON assignment. The CON assignment of CAPRIN1 in dilute phase was transferred to CON spectra of CAPRIN1 in condensed phases.

Note that we used carbon-detected CON experiment to improve the spectral resolution of intrinsically disordered proteins and to circumvent the fast amide solvent exchange rate at pH 7.4 and 30 °C, since CON data do not rely on amide resonances and solvent exchange rates do not influence the quality of spectra, unlike for NH-HSQC. Maintaining a pH of 7.4 was necessary

because lowering the pH decreases the average negative charge of phosphate groups and affects the overall charge of pFMRP and its electrostatic-driven interaction with CAPRIN1. In experiments involving dilute phase samples, we acquired NH-HSQC spectra at pH 7.4 and 10 °C to slow down the amide solvent exchange rate as shown in Figure S6. In experiments involving condensed phase samples, lowering the temperature to 10 °C drastically increases the viscosity of condensed-phase samples and leads to severe peak broadening.

NMR Analysis

NMRPipe (35) and CcpNmr Analysis 2.4.2 (36) were used for processing and analyzing NMR spectra. Peaks in NH-HSQC spectra were picked using CcpNmr Analysis 2.4.2 and peak intensities of NH-HSQC with 50 or 95 μ M pFMRP were divided with peak intensities of NH-HSQC without pFMRP. For NMR spectral analysis of condensed phase samples, chemical shifts and peak intensities of peaks in CON spectra were obtained after picking peaks using CcpNmr Analysis 2.4.2. Initially, raw intensity ratios were obtained by dividing peak intensities of pFMRP-CAPRIN1 and FMRP-CAPRIN1 condensed phase spectra with peak intensities of CAPRIN1 in buffer. Afterward, the raw intensity ratios were normalized for differences in NMR tubes (3 vs 5 mm tubes) used in each experiment and concentrations of [^{13}C , ^{15}N]CAPRIN1 in the dilute (~1 mM) and condensed phase samples (~3 mM) obtained from gel filtration. After converting chemical shift perturbations (CSPs) from ppm to Hz using their Larmor frequencies at 800 MHz magnetic field, the combined CSPs were calculated using $\sqrt{\delta_C^2 + \delta_N^2}$, where δ_C and δ_N are CSPs of carbon and nitrogen in Hz. Peak intensities and chemical shifts of residues 609, 613, 620, 662, 667, 671, 677, and 707 were not quantified due to limited spectral resolution and peak crowding. Residues 617, 685, 689, 691 were excluded from analysis due to their missing assignments.

Fluorescence Recovery After Photobleaching (FRAP)

FRAP experiments were performed on a Leica DM16000 SP8 Confocal microscope with a 63x/1.4 oil objective using a Hamamatsu C9100-13 EM-CCD Camera. A Cy5 labeled pFMRP sample (20 μ M) mixed with a FITC labeled CAPRIN1 sample (100 μ M) and sc1 RNA (5 μ M) in buffer containing 25 mM Na_2PO_4 pH 7.4 and 2 mM DTT was used to form droplets. Droplets were incubated at room temperature (~5 mins) and placed on glass bottom dishes (MatTek). A diameter of ~1-2 μ m was bleached for 1.4 seconds with 95% laser power at 649 nm to photobleach Cy5-pFMRP or 488 nm to photobleach FITC-CAPRIN1. A single confocal plane was maintained and images were collected for 30 seconds. Three regions of interests (ROI) were used for the FRAP analysis. ROI1 represents the bleached area within a droplet. ROI2 represents an unbleached area within a droplet used to correct for photobleaching due to laser illumination during image acquisition. ROI3 represents background signal which was subtracted from ROI1 and ROI2. Fluorescence recovery was obtained from ROI1 divided by ROI2 and then normalized and fitted to a single exponential function. Images were processed on Volocity (Perkin-Elmer) and ImageJ (NIH).

Condensate Surface Wettability Measurements

Surface wettability measurements were adapted from previous work (28). A 96-well glass-bottom plate (Eppendorf) was treated with either 1% Pluronic F-127 solution (Sigma Aldrich) or with Sigmacote (Sigma Aldrich). Solutions of Pluronic F-127 or Sigmacote were incubated on the plate for approximately 10 minutes producing either a hydrophilic or hydrophobic coating.

Excess solution was washed off with deionized water. The plate was dried with argon gas before use. FITC-labelled CAPRIN1 was mixed with either pFMRP to recapitulate the outer compartment or with sc1 RNA to recapitulate the inner compartment. These droplets were placed on top of the treated coverslips right before imaging. Z-stacks of droplets were acquired on a Leica DMI8 microscope equipped with Hamamatsu C9100-13 EM-CCD camera with a 60x objective. 3-D volume stacks were acquired and projected in the XZ plane to obtain the wetting shape profile. Contact angles were calculated using droplet height (h) and radius (r) measurements obtained on Image-J and using the following equation.

$$\theta = 2 \tan^{-1} \frac{h}{r}$$

***In vitro* deadenylation Assay**

In vitro deadenylation assays were adapted from (5). In brief, CNOT7 (final concentration of 5 μ M) was mixed with a 5'-FITC-PolyA₃₈ RNA (final concentration of 50 nM) and purified protein components (FMRP, pFMRP, CAPRIN1, pYCAPRIN1, pFMRP and CAPRIN1, FMRP and pYCAPRIN1, FMRP and CAPRIN1, or pFMRP and pYCAPRIN1) in a reaction buffer containing (25 mM NaPO₄ pH 7.4, 2 mM MgCl₂, 2 mM BME and 5% glycerol). Prior to adding CNOT7 and 5'-FITC-PolyA₃₈ RNA, droplets were pre-formed by mixing each component with the following concentration: CAPRIN1 (60 μ M), pYCAPRIN1 (60 μ M), FMRP (30 μ M), pFMRP (30 μ M). Reaction mixtures were incubated at 30 °C and quenched at specific time points by mixing in a 2x denaturing loading dye (95% formamide, 10 mM EDTA, 0.01% w/v bromophenol blue). Samples were boiled for 5 mins before loading onto a 6.5 M urea 20% TBE-polyacrylamide gel. Gels were run in 1x TBE buffer for ~2.5 hrs at a constant voltage of 100 V. After running, gels were directly scanned with a ChemiDoc MP System (BioRad) to detect 5'-FITC-polyA RNA cleavage. Gel images were analyzed using ImageJ to calculate deadenylation rates based on densitometric measurements of the appearance of cleaved 5'-FITC-PolyA₃₈ RNA as a function of time.

***In vitro* Translation Assay**

Luciferase mRNA (Promega) was translated using a nuclease treated Rabbit Reticulocyte Lysate System (Promega). Each reactions (30 μ L) contains 12.6 μ L of rabbit reticulocyte lysate, 0.5 μ L of Luciferase mRNA (1 mg/mL), 0.3 μ L of amino acid mixture minus leucine (1 mM), 0.3 μ L of amino acid mixture minus methionine (1 mM), and 16.3 μ L of 15 μ M protein, or buffer (25 mM NaPO₄ pH 7.4, 30 mM KCl, 2 mM DTT). Protein components used in the assay include FMRP, pFMRP, CAPRIN1, pYCAPRIN1, pFMRP and CAPRIN1, FMRP and pYCAPRIN1, FMRP and CAPRIN1, or pFMRP and pYCAPRIN1. Translation rates were monitored as the increase in luminescence as a function of time using a standard luciferase assay system (Promega). A standard reaction contained 75 μ L of luciferase substrate mixed with 2.5 μ L of unpurified translation mixture in a white opaque 96 well plate (Corning 3990). End-point luminescence measurements were carried out in five minutes time intervals up to 20 mins. Luminescence was detected using a SpectraMax i3x Multi-Mode Plate Reader (Molecular Devices) at 25 °C. Relative luminescence measurements represent mean values obtained from two independent *in vitro* translation reactions, each of them measured three times. The translation rates in the presence of different proteins were derived from fitting a line of best fit with the end-point luminescence readings as a function of time.

Turbidity Measurements

For turbidity measurements, OD600 readings of CAPRIN1 + pFMRP (or pFMRP-Alexa488) samples were obtained using a BioPhotometer (Eppendorf). The samples were prepared by mixing CAPRIN1 with pFMRP (or pFMRP-Alexa488) immediately before reading 5 μ L of the mixture using a μ Cuvette G1.0 (Eppendorf). Measurements were done in triplicate. Concentrations of CAPRIN1 and pFMRP (or pFMRP-Alexa488) were 200 and 30 μ M, respectively.

Bioinformatic Analysis

To test the correlation between tyrosine phosphorylation patterns and phase separation we first identified 18292 human protein sequences from the PhosphoSitePlus PTM database (22) that match the minimum sequence length required for phase separation prediction (140 residues) by the PScore algorithm based on long-range planar pi contacts (9), and then binned these sequences into 9 groups according to the maximum number of tyrosine phosphorylation sites found within a window length of 140 residues, matching the minimum protein size, where the first eight bins correspond to discrete numbers of phosphorylation sites (0 to 7, with Ns of 7054, 5222, 2949, 1528, 757, 348, 202, and 112) and the final bin consists of all proteins with 8 or more sites, including CAPRIN1 (N=120).

Correlation with phase separation prediction was tested by comparing the percentage of proteins in each bin that satisfy our predictor's standard confidence threshold (PScore \geq 4.0), as per (9). Enrichment statistics for gene ontology database annotations of biological function were tested using the PANTHER14.0 standard statistical overrepresentation test (37) against the "GO biological process complete" annotation set, with enrichment statistics calculated for each bin by treating them as independent sets. Statistical significance was calculated using Fisher's exact test.

Supplementary Text

Model system of FMRP, CAPRIN1 and RNA

The low-complexity regions of FMRP (445-632) and CAPRIN1 (607-709) were used in this study for multiple reasons. First, the relatively small sizes of these constructs make them ideal for NMR spectroscopy and structural characterization of the phase-separated state. Second, a phase separation prediction algorithm based on sequence compositions and π - π interactions (9) predicts that these low-complexity regions are sufficient to phase separate by themselves (fig. S2). Experimental evidence has confirmed that the low-complexity region of FMRP is indeed sufficient to phase separate *in vitro* and that truncation of this region from the full-length protein inhibits phase separation *in vitro* (18). In the case of CAPRIN1, truncation of the 607-709 low-complexity region prevents granule formation upon overexpression in cells (15, 21). Third, FMRP and CAPRIN1 are known interacting partners involved in similar functional processes including mRNA transport in neurons, mRNA stability, translational regulation and stress granule formation (13–15). Moreover, both proteins are involved in biological processes related to learning and long-term memory formation (16–18) and mutations in both proteins are associated with neurodevelopmental disorders (17, 38).

Multivalency is a key determinant underlying phase separation (1, 2). Thus, we envision that the folded domains in FMRP and CAPRIN1 will affect their phase separation propensities. Specifically, the homodimer domain of CAPRIN1 and the KH RNA binding domain and Agenet (Tudor) domains in FMRP could modulate phase separation via protein-protein or protein-RNA interactions. The crystal structure of the CAPRIN1 dimerization domain shows the possibility of FMRP and mRNAs to interact with this domain in a multivalent fashion (39). Similarly, the RNA-binding domains and the Agenet domains of FMRP can increase its multivalency by facilitating multiple protein-RNA and protein-protein interactions. Interestingly, the Agenet domains are known to bind methylated arginine or lysine residues which highlights the importance of post-translational modifications in phase separation (40, 41). Likely the synergy between these folded domains and the LCRs can contribute to binding specificity of certain components and affect the biochemistry occurring within condensates.

To investigate the effect of RNA in our condensates, we used sc1 RNA, which is an *in vitro* selected 36-mer RNA that forms a well-characterized three-layered G-quadruplex-linked to a duplex stem (27). Sc1 RNA has been shown to interact with RGG/RG motifs (42) that are present in the low-complexity regions of FMRP and CAPRIN1 used in this study. Indeed, FMRP and CAPRIN1 can both individually phase separate with sc1 (fig. S2C and D). We note that G-quadruplex structure is not required to form multi-phasic sub-compartments of pFMRP-CAPRIN1-RNA condensates as sub-structure formation is observed with poly(A)₃₈ RNA (Fig. 4B). We expect that pFMRP with CAPRIN1 and luciferase RNA can form multi-phase compartments if there is not a strong dependence on RNA length, but this could not be ascertained due to lack of fluorescence tags in the translation experiment.

In vitro model with CNOT7

In our *in vitro* model system, we used CNOT7, a catalytic subunit of the CCR4-NOT complex which is a multiunit complex regulating eukaryotic gene expression (43). Our *in vitro* data suggests that specific condensate protein compositions and PTM states can regulate CNOT7 activity. In terms of function, CNOT7 localizes to punctate structures in neurons and regulates local translation and mRNA transport (29), which overlaps with the localization and activities reported for FMRP and CAPRIN1 (16–18). Although the activity of isolated CNOT7 can be

controlled by phase separation *in vitro*, it remains unclear how it behaves in the context of an intact megadalton CCR4-NOT complex. Note, many of the non-catalytic components of the CCR4-NOT complex are known to tether the complex to mRNA by forming specific interactions with RNA-binding proteins (44).

NMR spectra of CAPRIN1

There are two regions (621-635 and 681-692) of CAPRIN1 that give rise to minor populations with two NMR resonances, with the first region likely due to the natural chemical modification that changes asparagine followed by glycine into iso-aspartic acid (isoAsp) (45). The second region of minor populations is likely due to cis-trans proline isomerization (P683, P687, P693, P694, and P696).

When CAPRIN1 is placed in a condensed phase of FMRP or pFMRP, we noticed consistent ^{13}C and ^{15}N upfield-shifted chemical shifts by ~16 and ~13 Hz, respectively. We believe that the systematic chemical shifts arise from the unique solvent environment in condensed protein phases that have previously been shown to be partially solvent-depleted (25). Supportive of this, when we examine the water-line position in samples of CAPRIN1, there is an 18 Hz downfield shift of water in the condensed phase relative to the dilute sample. The unique and solvent-depleted environment of a condensed protein phase is also predicted to have a lower dielectric constant (25) that can enhance electrostatic interactions, such as those between FMRP and CAPRIN1, compared to buffer.

Protein interactions in NMR and other experiments

For NMR interaction experiments, we used [^{13}C , ^{15}N]CAPRIN1 in an FMRP condensed phase to compare to those in a co-phase-separated state with pFMRP. We do not detect interactions or co-phase separation with CAPRIN1 and FMRP even at millimolar concentrations (fig. S4, C and D), unlike the clear interaction and co-phase separation between CAPRIN1 and pFMRP at low micromolar concentrations (fig. S4, B and C). Thus, we partitioned [^{13}C , ^{15}N]CAPRIN1 into a pre-formed FMRP condensate representing protein partitioning into condensates, *i.e.*, CAPRIN1 acts like a “passenger” or “client” while [^{13}C , ^{15}N]CAPRIN1 – pFMRP condensates represent co-phase separation, *i.e.*, both proteins “drive” phase separation as “scaffolds” (46).

Intensity ratios upon interactions of disordered proteins are interpreted as being largely dominated by dynamic interactions, with resonance broadening due to dynamic changes in the chemical environments (and thus chemical shifts) due to exchanging interactions on the millisecond to microsecond timescale, as described previously (47). Moreover, we suspect that the small chemical shift differences of CAPRIN1 in pFMRP or FMRP condensed phases are similarly due to the transient and dynamic nature of the interaction between these IDPs. The aromatic-rich regions of CAPRIN1 exhibit the largest reductions of intensity ratios in both FMRP and pFMRP condensed phases compared to the intensities of CAPRIN1 in buffer. We interpret this to mean that the aromatic-rich regions play a general role in the partitioning of CAPRIN1 into both FMRP and pFMRP condensed phase via interactions with π groups in FMRP and pFMRP. The arginine-rich region has dramatic but smaller reductions of intensities in the condensed phases (with FMRP or pFMRP) compared to dilute CAPRIN1, but significant differences between the FMRP and pFMRP condensed phases, pointing to more arginine interactions with pFMRP.

Viscosity effects due to very high protein concentrations in the condensed phase also contribute to intensity ratios when compared to buffer. However, since FMRP and pFMRP

condensed phases have similar measured concentrations (fig. S7C), the effect of viscosity on [^{13}C , ^{15}N]CAPRIN1 intensity ratios when comparing between FMRP and pFMRP condensed phases should be negligible. Note that most of our experiments are performed with 25 mM phosphate buffers (~50 mM ionic strength), enhancing the electrostatic contributions relative to physiological salt conditions. Also, we do not use synthetic crowding reagents (such as PEG and Ficoll) in our study.

Comparison to previous FMRP model

Our general hypothesis is that phase separation represents an organizing mechanism to mediate coupled biological processes such as translation and deadenylation and that changes in condensate compositions and PTM states can modulate these processes. To test our hypothesis, we performed both deadenylation and translation assays. In contrast to the conditions used in our previous translation assays with FMRP alone (18), we utilized much higher FMRP/pFMRP concentrations; at these high concentrations, as observed here and as previously shown (18), the translation inhibition effect of FMRP and pFMRP is similar. We note that FMRP with a high number of phosphorylation sites (~9) did not show simple droplet formation in rabbit reticulocyte lysate, potentially implying gelation or aggregation (fig. S20C), consistent with its poor biochemical behavior. We also note that the *in vitro* translation system uses uncapped luciferase mRNA. Addition of CNOT7 would affect cap-dependent translation initiation but likely not cap-independent translation. Thus, CNOT7 does not inhibit luciferase mRNA translation in our system.

Functional roles of phosphorylation of FMRP and CAPRIN1

Previous work has shown that S/T phosphorylation of FMRP inhibits translation (18). FMRP is also involved in mRNA stability, but how the phospho-state affects stability remains unclear. For CAPRIN1, although multiple (up to 5) tyrosines are detected to be phosphorylated (22), their functional role has not been studied beyond this work. By conducting a bioinformatic analysis, we show that multi-site tyrosine phosphorylation correlates both with the predicted propensity to phase separate (fig. S10A) and with protein functional annotations involving regulation of translation and mRNA stability (fig. S10B), suggesting a possible general relationship for tyrosine phosphorylation in regulating phase separation behavior. While the vast majority of these phosphorylation events have not been studied to identify function, the potential for multi-site tyrosine phosphorylation to control phase separation in the context of translational regulation can be identified in a number of proteins that, like CAPRIN1, are either known or predicted to phase separate (fig. S10D, Table S1). Similarly to CAPRIN1, these Tyr phosphorylation sites often occur in the context of RGG elements whose function involves RNA binding. The presence of tyrosine phosphorylation sites in CAPRIN1's RGG-containing C-terminus leads to reduced RNA binding affinity upon phosphorylation (fig. S11), but this is not enough to explain how phase separation affects enzyme activity and localization of both protein and RNA. Thus, multiple effects of Tyr phosphorylation on RNA and other binding events, phase separation, and enzymatic regulation likely contribute to biological function.

Role of phase separation in regulating *in vitro* deadenylation and translation

Is phase separation necessary for modulating deadenylation and translation, or is phase separation a consequence (bystander effect) of binding interactions? Here, we demonstrate that *in vitro* deadenylation rates by CNOT7 is not changed by CAPRIN1 binding without phase

separation. Indeed, CAPRIN1 and CNOT7 co-phase separation are needed to alter its enzymatic activity. We speculate that within a CAPRIN1 condensate environment that partially solvates CNOT7, CAPRIN1 may contribute specific interactions that can modulate CNOT7 conformation and dynamics. For example, CAPRIN1-RNA sub-compartments (within pFMRP-CAPRIN1-RNA condensates) have a similar composition to CAPRIN1-RNA condensates and thus exhibit similar deadenylation activities (Fig. 4D). In contrast, a different condensate composition such as FMRP-RNA or FMRP-pYCAPRIN1 have drastically different deadenylation activities (Fig. 4D). Thus, differences in condensate compositions and protein PTM states could alter CNOT7 activities.

For translational regulation, we intuit that one simple and effective approach to inhibit translation is to segregate mRNAs from the translation machinery or to segregate some components of the translational machinery from others. As a proof-of-concept, we show that the eukaryotic translation initiation factor 4E (eIF4E), a critical regulator of translation (30), is segregated from polyA-RNA within CAPRIN1-pFMRP condensates. We propose that different condensate compositions and PTM states could change partitioning affinities that could, in turn, modulate translation. Note that our rabbit reticulocyte lysate translation assay utilizes uncapped luciferase mRNA, which would be translated in a cap-independent manner. There have been significantly fewer studies of the role of eIF4E in cap-independent translation initiation, but there is strong evidence for the importance of eIF4G (48) and some evidence for that of eIF4E (49). As eIF4E binds eIF4G, our eIF4E fluorescence data could be viewed as a surrogate for eIF4G, with both partitioning away from the RNA to inhibit translation. While partitioning to segregate essential components of the translational machinery and RNA is a simple, elegant mechanism for translation inhibition, there are possibly other mechanisms at play.

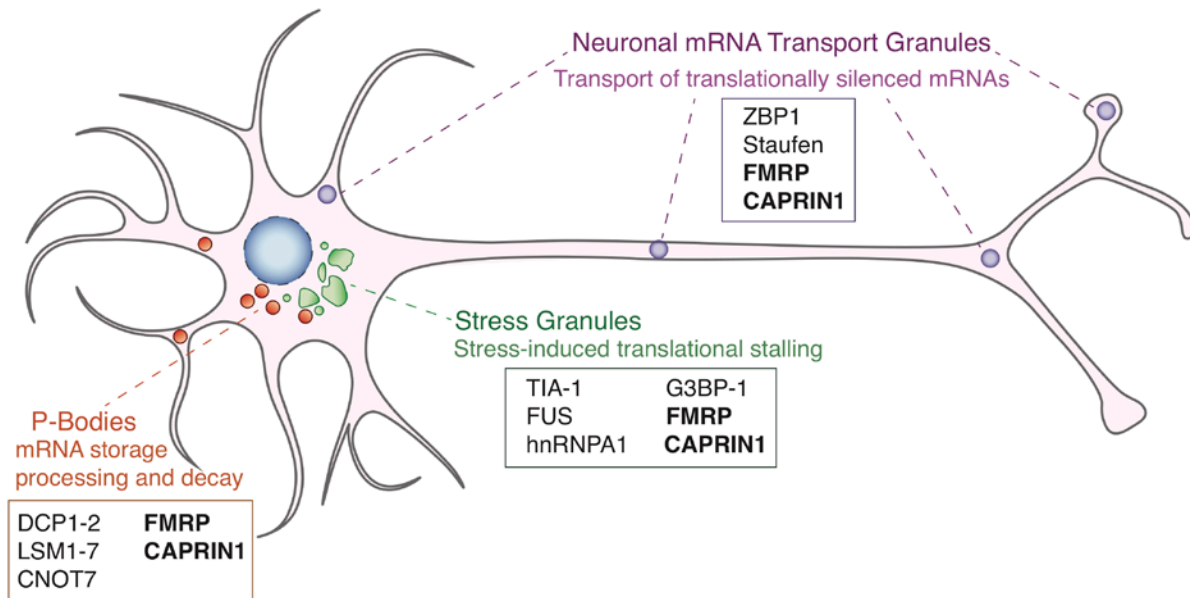


Fig. S1. Cartoon representation of three common cytoplasmic condensates in neurons. Three common neuronal cytoplasmic condensates include neuronal transport granules, P-bodies and stress granules (10, 50). Examples of proteins identified in each condensate are listed in corresponding boxes. FMRP and CAPRIN1 represent proteins shared between condensates.

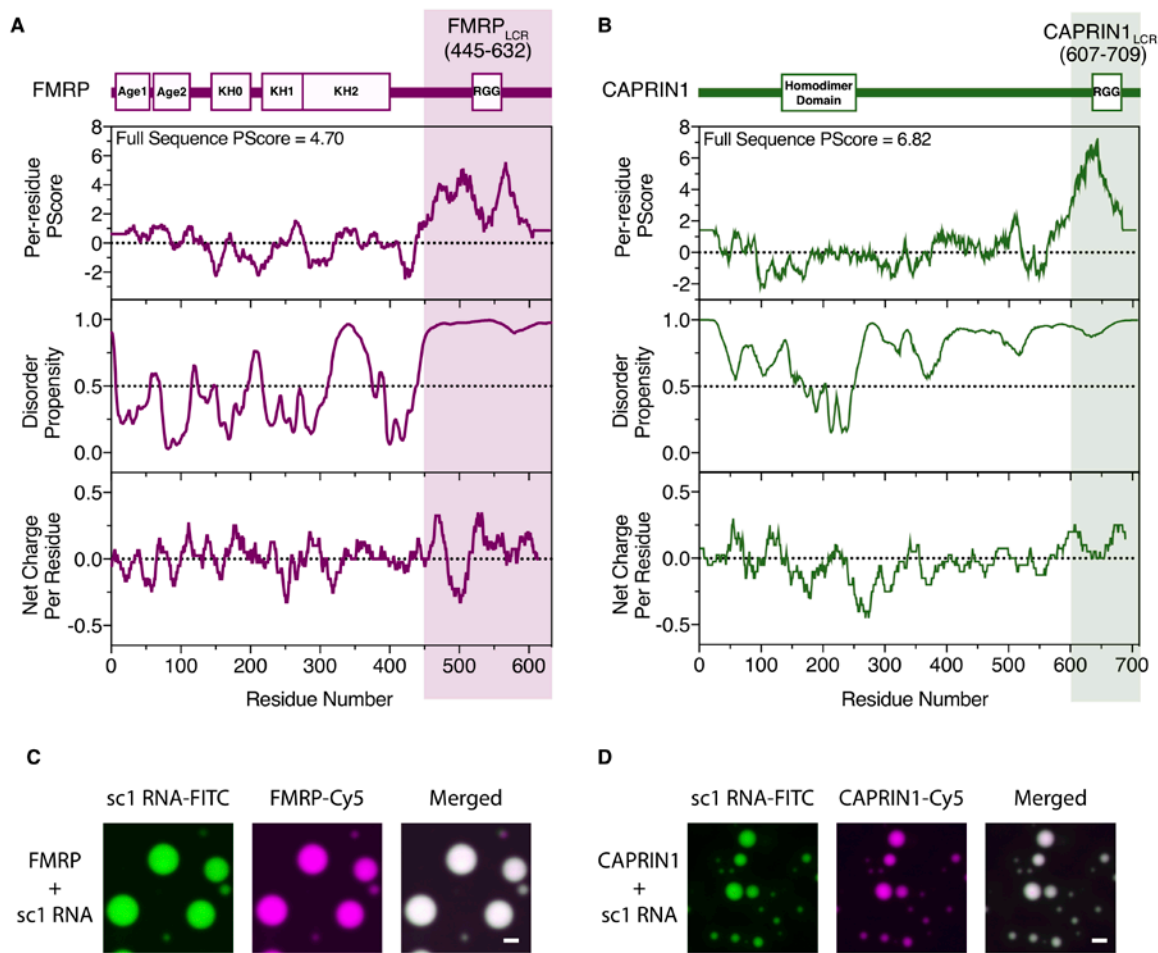


Fig. S2. The C-terminal low-complexity regions (LCRs) of FMRP and CAPRIN1 are predicted to phase separate and be disordered based on sequence composition, and readily phase separate with RNA *in vitro*. (A) The LCR of FMRP (445-632) used in this study contains RGG/RG repeats. It was previously shown to phase separate, having been predicted to do so using a defined method that predicts phase separation with a score threshold of “PScore” ≥ 4.0 (9). It is predicted to be intrinsically disordered (51) and contains a pattern of positive and negative charge blocks (sliding residue window = 20). FMRP also contains two Agenet (Age1, Age2) methyl-lysine-binding and three K homology (KH0, KH1, KH2) RNA-binding domains. (B) The LCR of CAPRIN1 (607-709) used in this study also contains RGG/RG repeats. It is predicted to phase separate, predicted to be disordered (51) and contains an overall net positive charge (sliding residue window = 20). CAPRIN1 has a folded homodimerization domain, but is otherwise predicted to be intrinsically disordered. (C, D) Fluorescence images of the FMRP and CAPRIN1 LCRs with sc1 RNA show phase separated droplets. Scale bar is 2.5 μm . Concentration of FMRP and CAPRIN1 was 100 μM . sc1 RNA concentration was 5 μM .

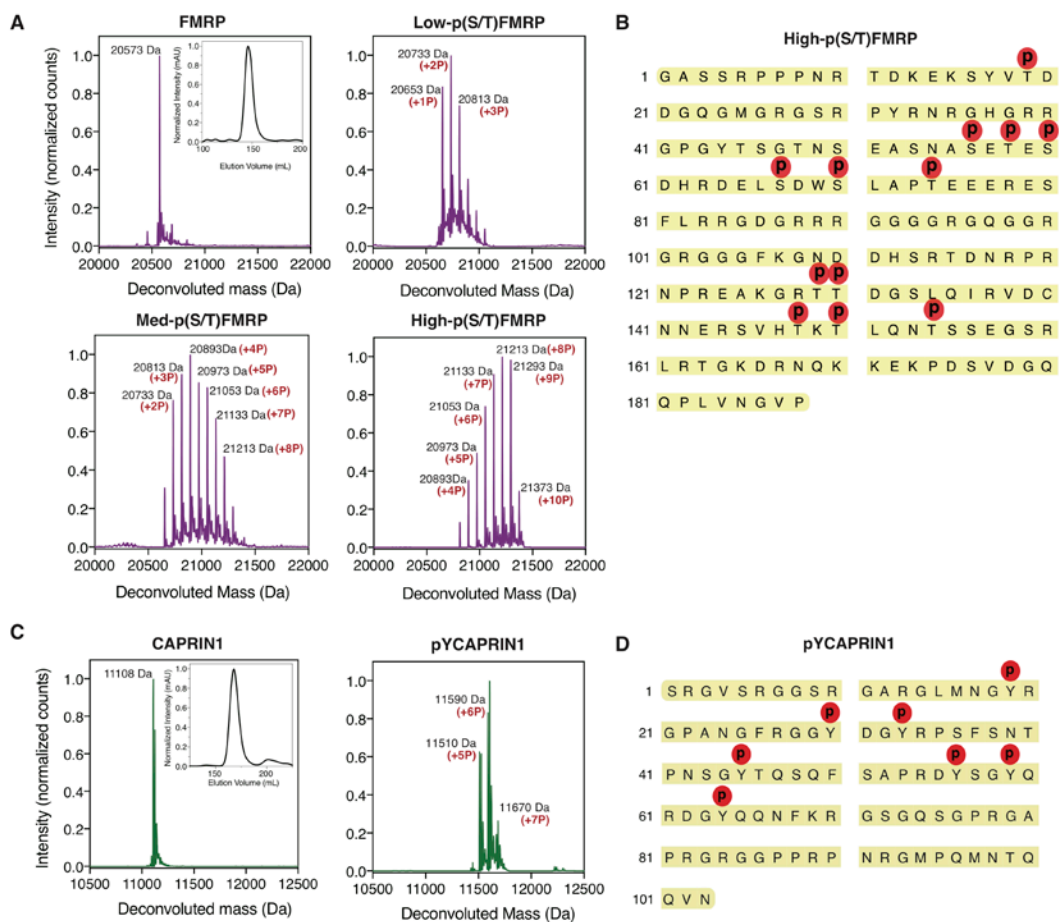


Fig. S3. Intact mass spectrometry and LC-MS/MS spectrometry of phosphorylated FMRP and CAPRIN1. (A) Intact mass spectra of FMRP before and after variable times of phosphorylation with CK2. Inset in FMRP mass spectrum is a gel-filtration profile of FMRP. Phosphorylated residues coincide with the reported CK2 phosphorylation motif which contains Ser/Thr residues adjacent to acidic residues (52). (B) Positions of phosphorylation sites in pFMRP with varying degree of phosphorylation revealed by LC-MS/MS. Our *in vitro* phosphorylation overlaps with 5/8 pSer/pThr FMRP PhosphoSitePlus annotations (22). Numbering begins from the FMRP C-terminal region residue 445. (C) Intact mass spectra of CAPRIN1 before and after tyrosine phosphorylation by Eph4A. Inset in CAPRIN1 mass spectrum is a gel-filtration profile of CAPRIN1. (D) LC-MS/MS shows positions of phosphorylation sites in pYCAPRIN1. Our *in vitro* phosphorylation overlaps with all 5 of the pTyr CAPRIN1 PhosphoSitePlus annotations (22), with additional sites phosphorylated. Note as well that there are additional PhosphoSitePlus annotations outside of the FMRP and CAPRIN1 LCRs used in this study. Numbering begins from the CAPRIN1 C-terminal region residue 607.

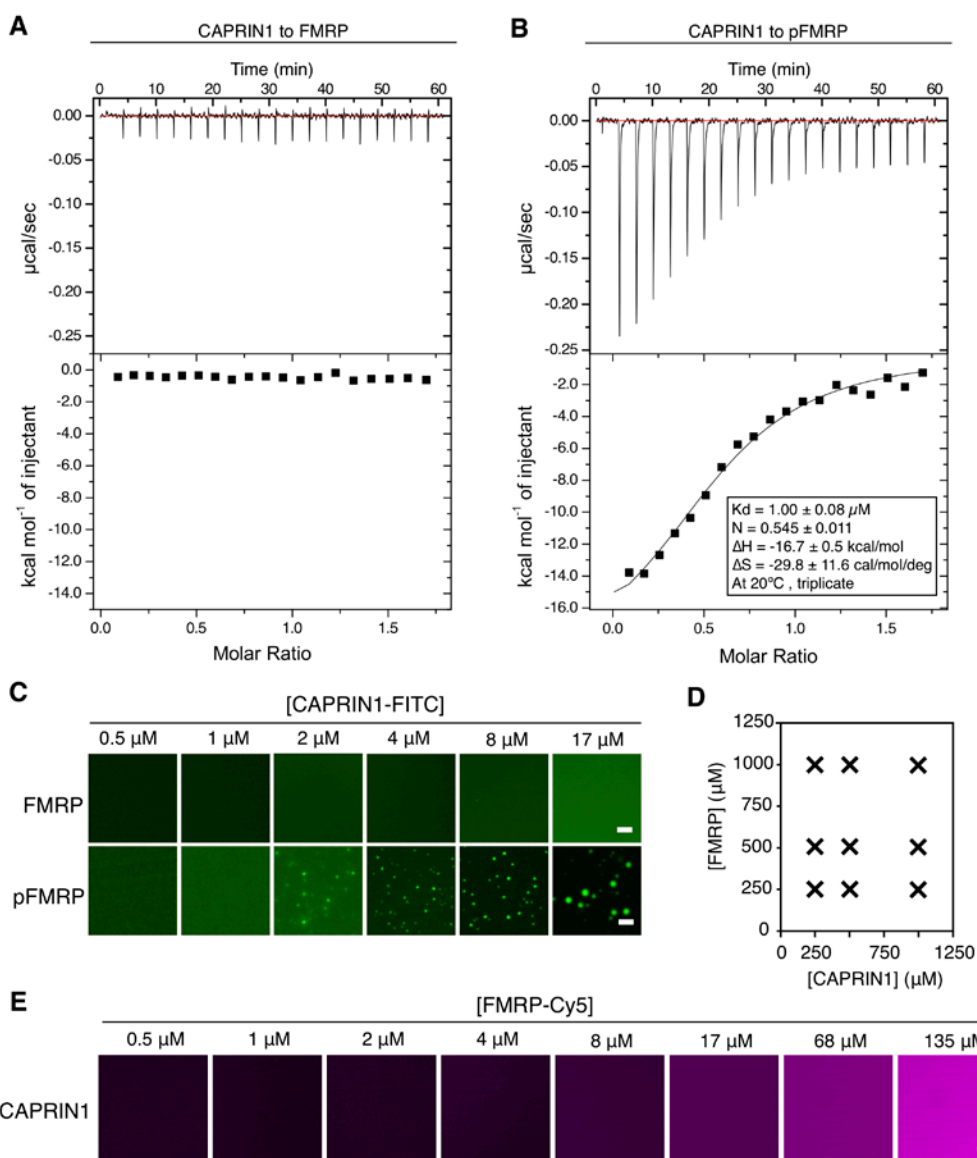


Fig. S4. FMRP interacts with CAPRIN1 in a phosphorylation-dependent manner.

(A) Representative ITC curve of CAPRIN1 (95 μM) titrated into FMRP (10 μM) in buffer containing 25 mM NaPO₄ pH 7.4 and 2 mM β -Mercaptoethanol (βME). (B) Representative ITC curve of CAPRIN1 (95 μM) titrated into pFMRP (10 μM , average of 9 phosphorylation sites) in buffer containing 25 mM NaPO₄ pH 7.4 and 2 mM βME . (C) Representative images of ITC data points show formation of droplets during ITC titration of pFMRP. CAPRIN1-FITC was titrated into 10 μM FMRP or high pFMRP. (D) Phase diagram of FMRP and CAPRIN1 shows absence of droplets even at 1.0 mM protein concentrations. (E) Fluorescence images of CAPRIN1 with increasing concentration of FMRP-Cy5 show absence of droplets. Cy5-labelled FMRP was titrated into 10 μM CAPRIN1. Scale bar is 4.8 μm .

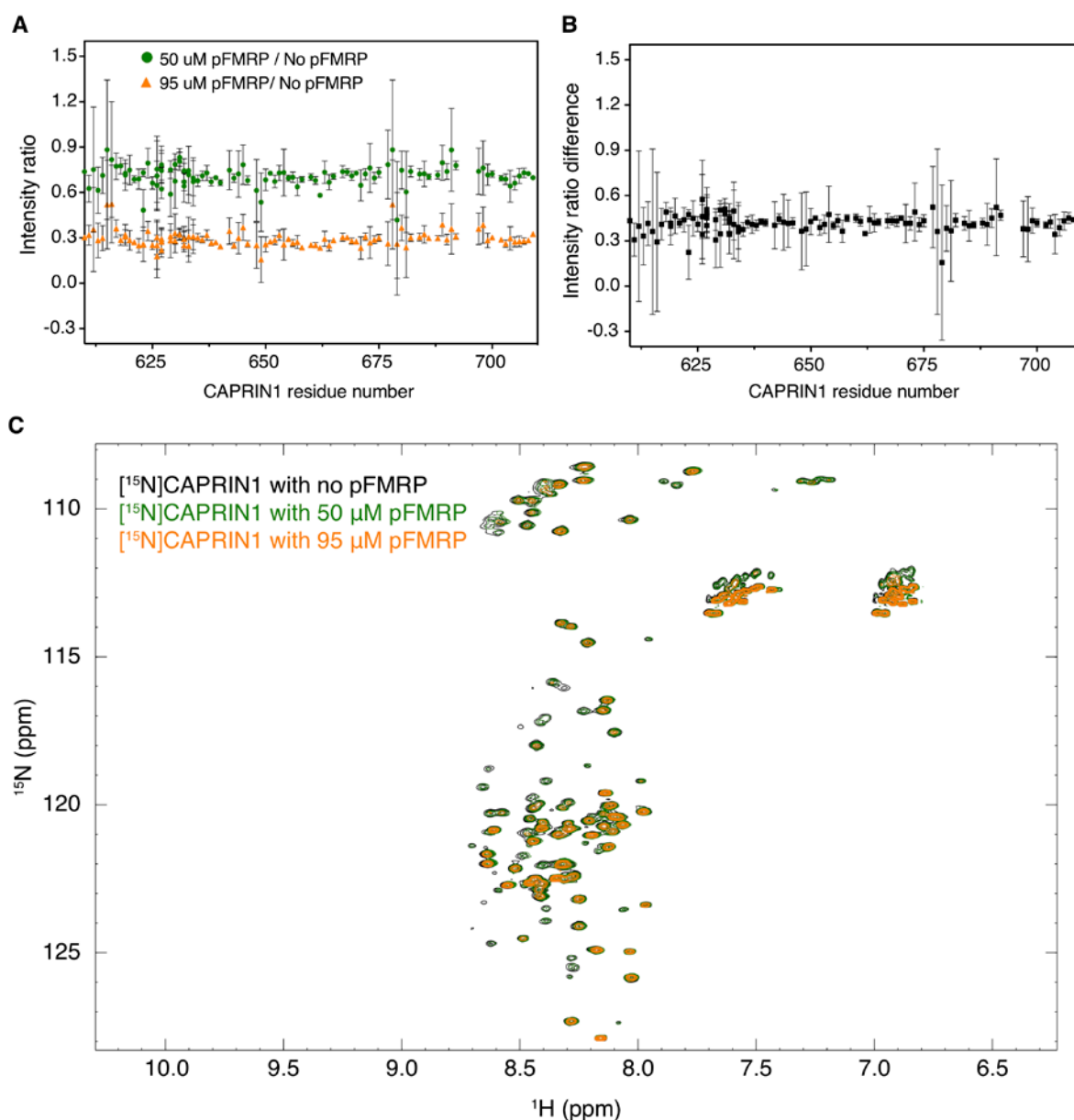


Fig. S6. NH-HSQC of ^{15}N CAPRIN1 titrated with pFMRP results in global decrease in intensities without chemical shift perturbations, supportive of interaction only within the phase-separated state. (A) Intensity plots of 100 μM of ^{15}N CAPRIN1 titrated with 50 μM pFMRP or 95 μM pFMRP each divided by ^{15}N CAPRIN1 in buffer containing 25 mM NaPO_4 , pH 7.4, 10 mM TCEP and 10% D_2O . Experiments were performed at 10 $^\circ\text{C}$. (B) Subtraction between 0.5:1 molar ratio of pFMRP to ^{15}N CAPRIN1 with ~ 1:1 molar ratio of pFMRP to ^{15}N CAPRIN1 shows no intensity differences. (C) Overlay of NH-HSQC spectra monitoring pFMRP titrations into 100 μM ^{15}N CAPRIN1 shows no chemical shift perturbations.

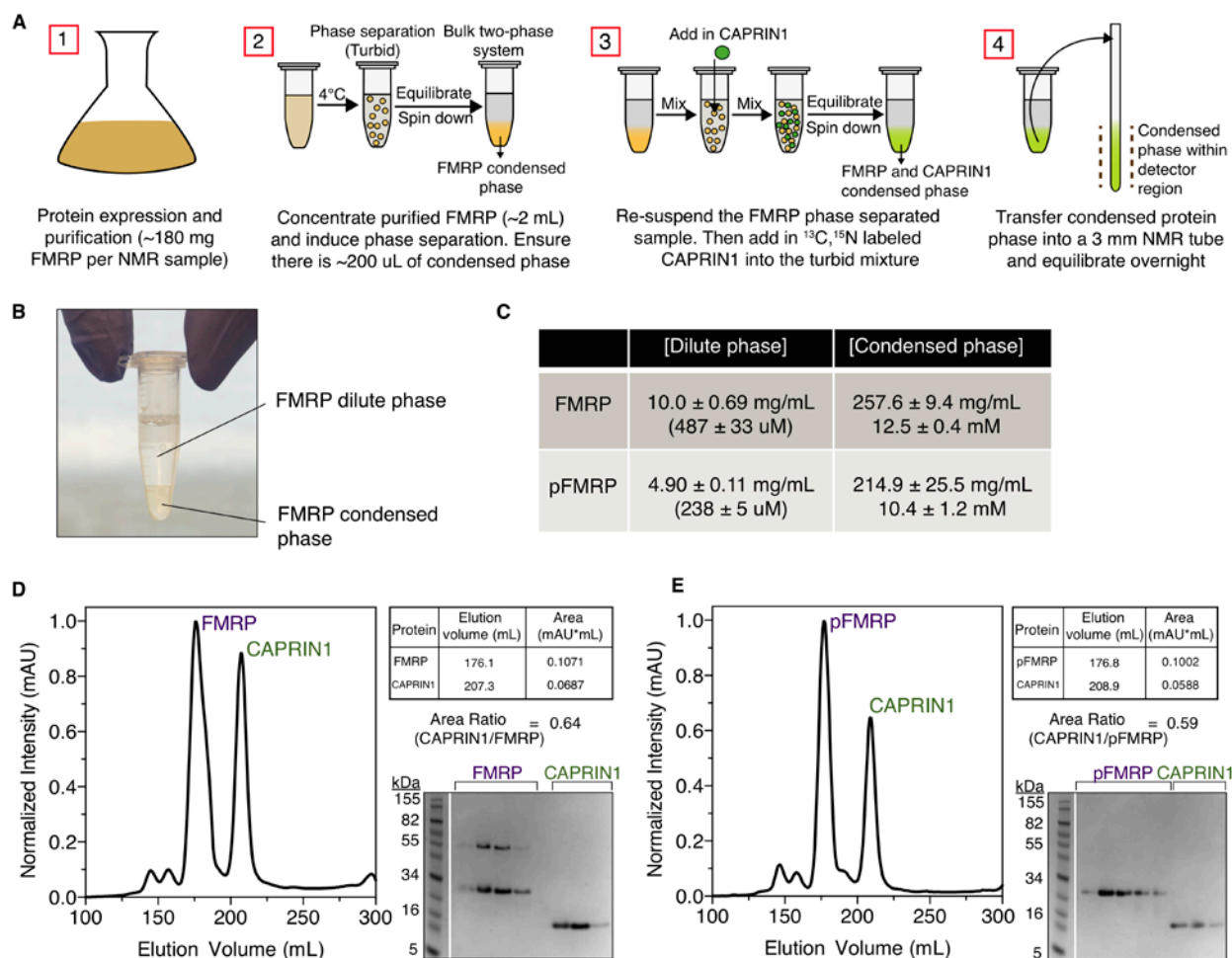


Fig. S7. Preparation and concentration measurements of condensed phase NMR samples.

(A) Schematic diagram for preparation of NMR condensed phase samples. In brief, we first induced FMRP or pFMRP to phase separate into a bulk two-phase system containing a protein-depleted phase on top and a protein-condensed phase (~200 μ L) on the bottom, similar to a tube mixed with water and oil. [^{13}C , ^{15}N]CAPRIN1 was rigorously mixed with either the condensed FMRP phase or condensed pFMRP phase. The samples were transferred to 3 mm NMR tubes, ensuring that the condensed phase volume was within the NMR detector region. (B) Photograph of an example bulk condensed phase. (C) Concentrations of the dilute and condensed phases calculated from A280 measurements of each phase. (D, E) Gel filtration of the FMRP-CAPRIN1 (D) and pFMRP-CAPRIN1 (E) condensed phases. Relative concentrations of FMRP/pFMRP and CAPRIN1 were calculated from the ratio of the two gel filtration peaks. CAPRIN1 experiences similar concentrations of FMRP/pFMRP in the two samples. The upper band of FMRP in the gel in panel D is a cysteine cross-linked dimer of FMRP due to the lack of reducing reagent in the gel buffer; note that all buffers for experimental samples contained reducing reagent (see Materials and Methods).

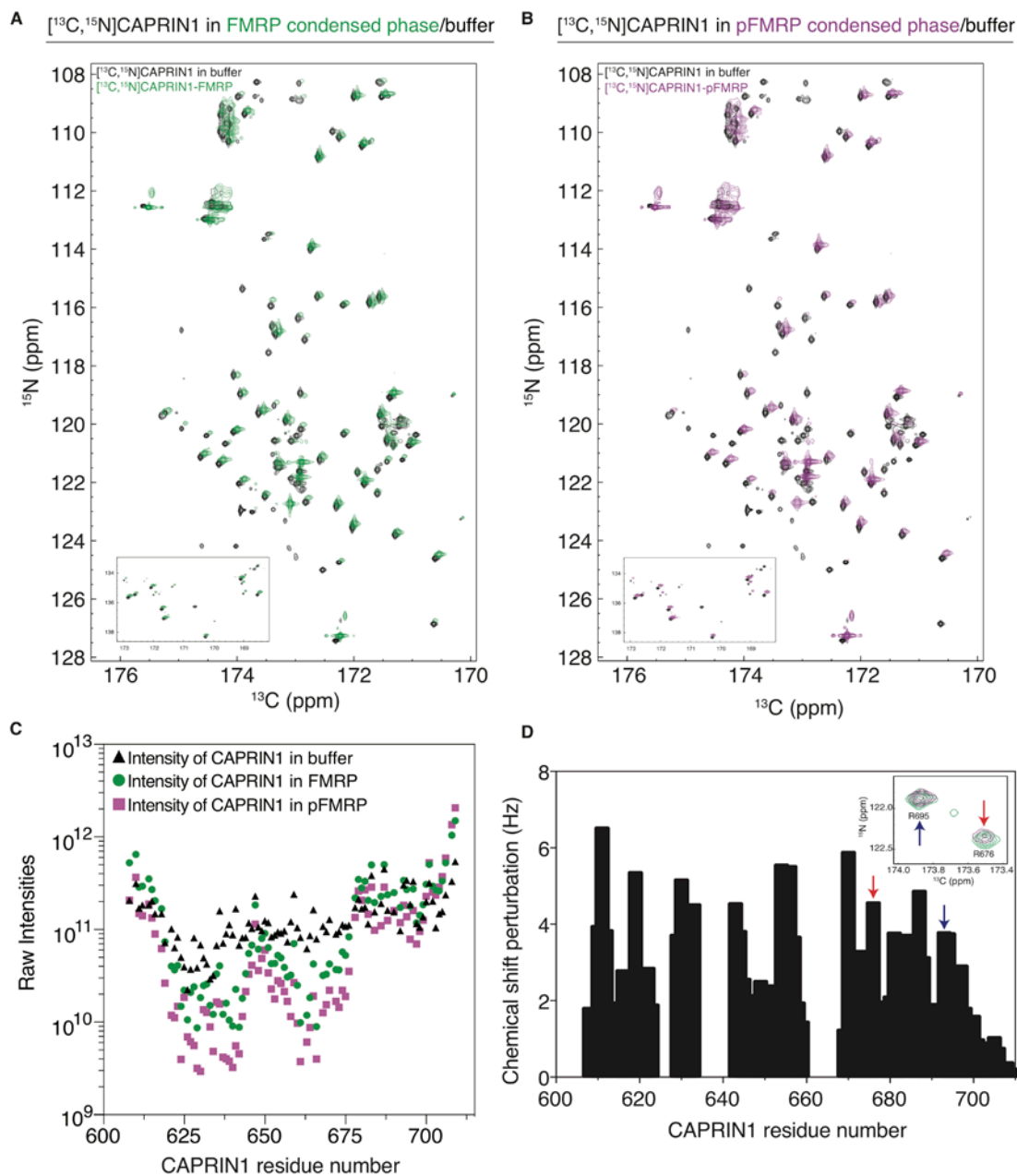


Fig. S8. CON spectra of $[^{13}\text{C}, ^{15}\text{N}]$ CAPRIN1 in FMRP or pFMRP condensed phases and in buffer. (A) CON spectrum of $[^{13}\text{C}, ^{15}\text{N}]$ CAPRIN1 in condensed FMRP phase (green) superimposed on a spectrum of $[^{13}\text{C}, ^{15}\text{N}]$ CAPRIN1 in buffer (black) containing 25 mM NaPO_4 pH 7.4 and 5 mM TCEP. Experiments were performed at 30 °C (B) CON spectra of $[^{13}\text{C}, ^{15}\text{N}]$ CAPRIN1 in condensed pFMRP phase (magenta) superimposed on a spectrum of $[^{13}\text{C}, ^{15}\text{N}]$ CAPRIN1 in buffer (black) containing 25 mM NaPO_4 pH 7.4 and 10 mM TCEP. (C) Raw intensities from each CON peak plotted as a function of residue number based on assignments before accounting for different protein concentrations and NMR tubes (see

Materials and Methods). **(D)** Differences in chemical shifts between CON spectra of CAPRIN1-FMRP and CAPRIN1-pFMRP condense phases. Chemical shifts of peaks with low intensities were excluded. R695 (blue arrow) and R676 (red arrow) peaks are shown as representative examples of small chemical shift changes. Residues with low intensities (624-628, 633-642, and 660-668) were excluded from CSP analysis. The residue numbers correspond to the N atom of CON resonances.

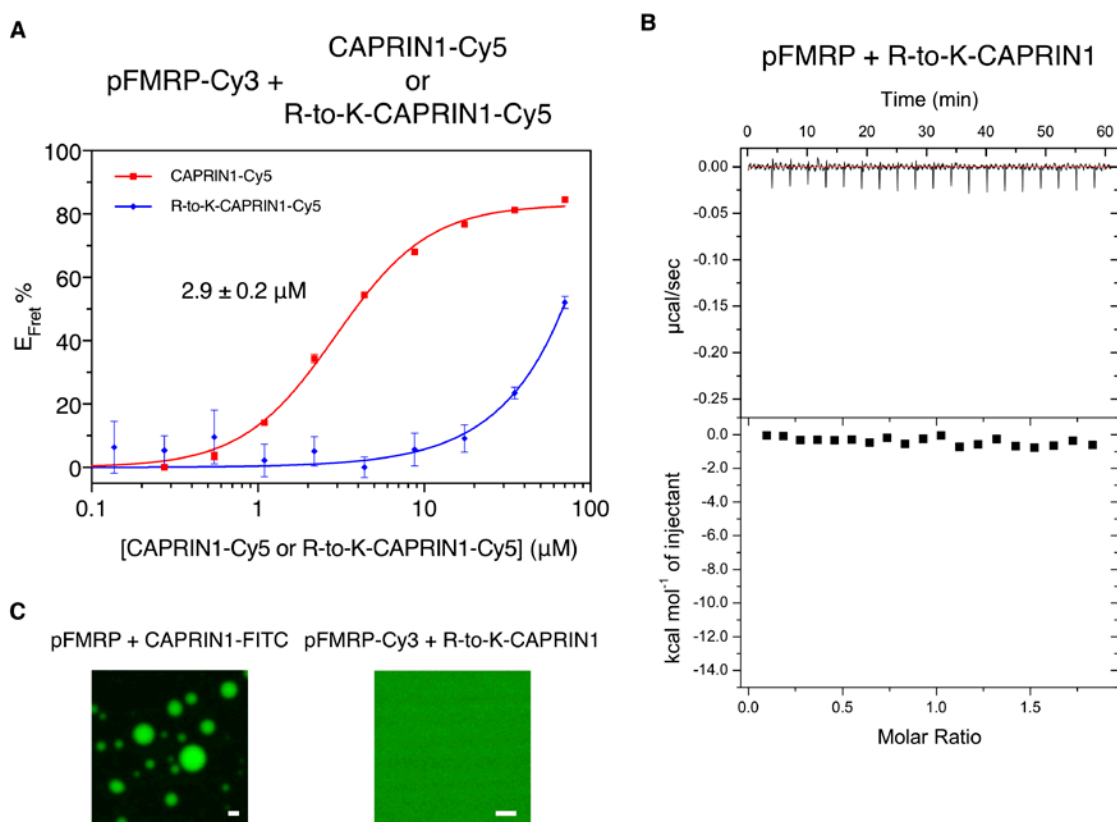


Fig. S9. R-to-K-CAPRIN1 mutation reduces binding affinity and perturbs co-phase separation with pFMRP. (A) FRET efficiency is significantly reduced when pFMRP-Cy3 is titrated with R-to-K-CAPRIN1-Cy5 compared to wild type CAPRIN1-Cy5. (B) ITC detects no heat changes for 100 μM R-to-K-CAPRIN1 titrated to 10 μM of pFMRP. (C) The absence of droplets with 10 μM of pFMRP-Cy3 mixed with 250 μM of R-to-K-CAPRIN1. An image of 10 μM of pFMRP with 68 μM of CAPRIN1-FITC is shown for comparison. Scale bars represent 2 μm .

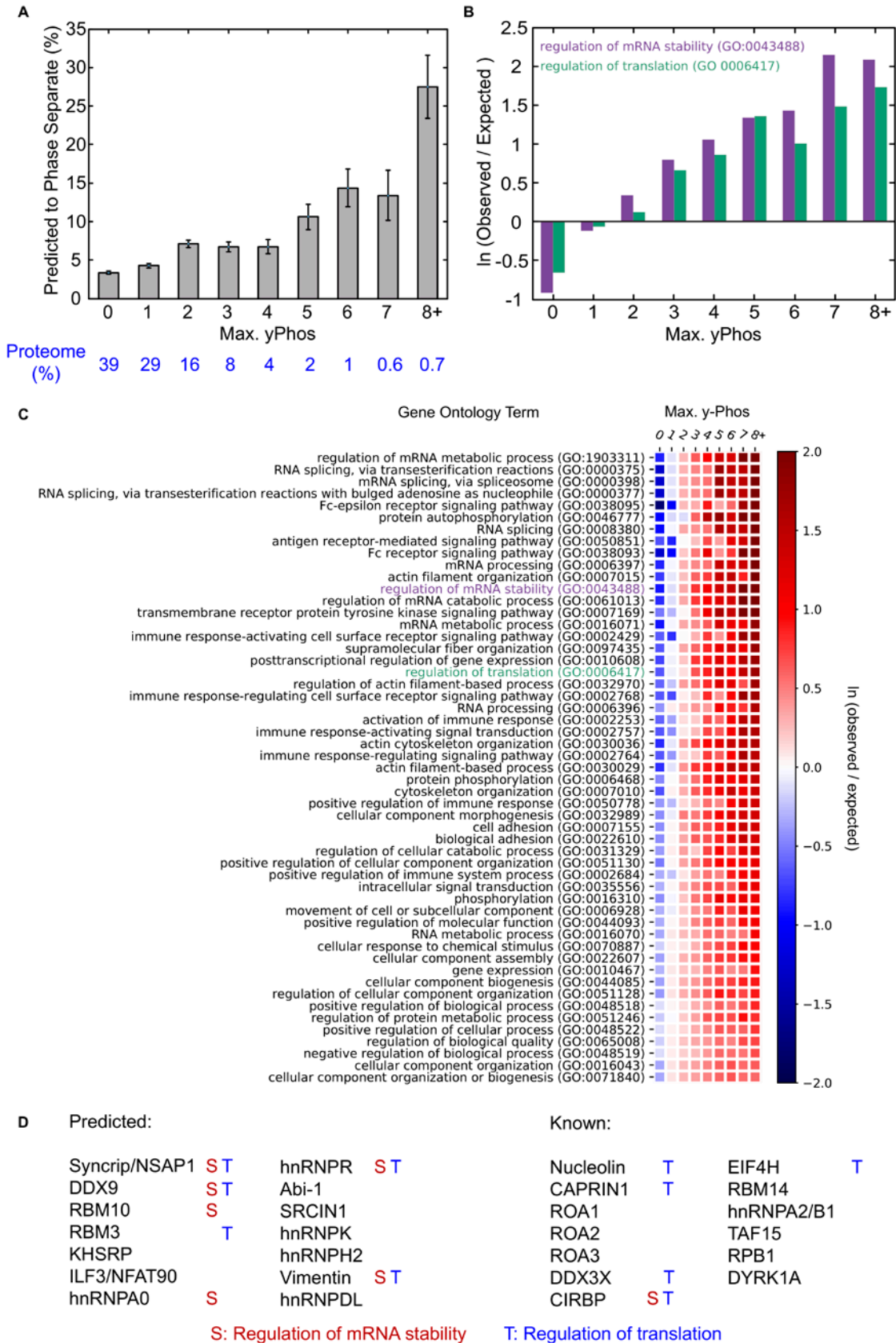


Fig. S10. Bioinformatic analysis of the association of tyrosine phosphorylation with phase separation and Gene Ontology terms. (A) Human proteins were binned according to the maximum number of tyrosine phosphorylation sites observed in the PhosphoSitePlus database over a 140-residue window, with the fraction in each bin shown in blue, and the upper limit of 8+ representing proteins with greater or equal numbers of tyrosine phosphorylation sites as CAPRIN1. The percentage of proteins predicted to phase separate using the PScore algorithm based on long-range planar pi contact (9) is shown for each category, demonstrating that proteins with regions of multi-site tyrosine phosphorylation are associated with increased likelihood of being involved in phase separation (error bars show standard error of the mean from bootstrap analysis). (B) Gene ontology functional annotation enrichment was measured using PANTHER14.0 for each independent set of binned proteins, and the annotation enrichment is observed to correlate with number of tyrosine phosphorylation sites for both regulation of mRNA stability and regulation of translation. (C) Enrichment correlation plots are shown as a heat map for all gene ontology biological function terms where the proteins with 8+ phosphorylation sites are significantly enriched and the proteins with 0 sites are significantly depleted (significance taken from PantherDB, using a threshold of $p < 0.00001$). (D) A selection of human proteins (from the 6, 7 or 8+ bins of max yPhos) that are either predicted to phase separate or known to phase separate are listed (see Table S1), with gene ontology annotations for mRNA stability or regulation of translation labeled.

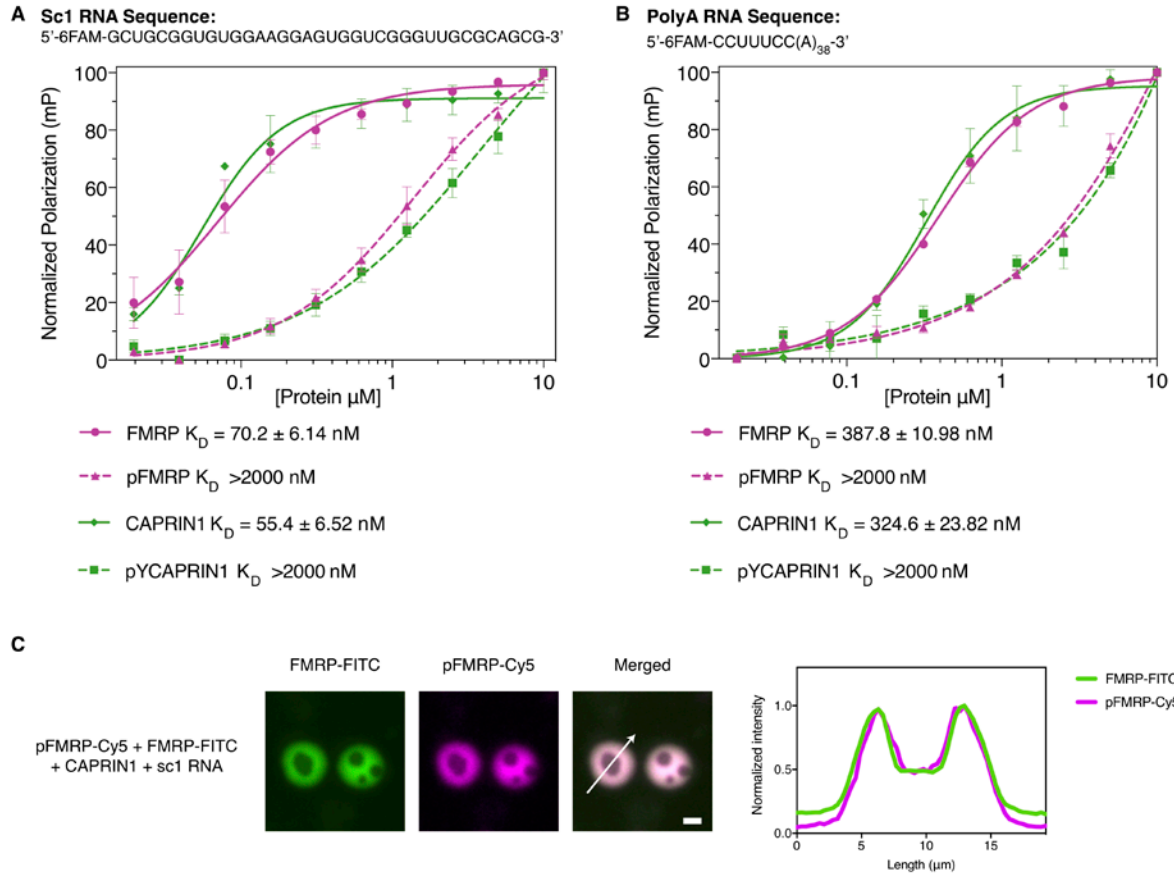


Fig. S11. Fluorescence polarization of sc1 and polyA RNAs used to quantify RNA affinities of FMRP and Caprin with/without phosphorylation. (A) FMRP and CAPRIN1 exhibit 50-70 nM K_D values, showing tight affinities for sc1 RNA. Phosphorylation reduces the RNA affinities to weaker than 2 μM . Sc1 RNA labelled with FITC at 5' was used for measuring the fluorescence polarization. (B) FMRP and CAPRIN1 have 320-390 nM affinities with polyA RNA. Phosphorylation reduces the RNA affinities to weaker than 2 μM . polyA RNA labelled with FITC at 5' was used for measuring the fluorescence polarization. (C) Fluorescence images of pFMRP-Cy5 + CAPRIN1 + sc1 RNA with FMRP-FITC show that FMRP-FITC is colocalized with pFMRP-Cy5 in the outer compartment, rather than RNA, even though it has similar RNA-binding affinity to CAPRIN1. Scale bar is 2 μm . CAPRIN1 and FMRP-FITC concentrations are 100 μM . pFMRP-Cy5 concentration is 30 μM . sc1 RNA concentration is 3 μM .

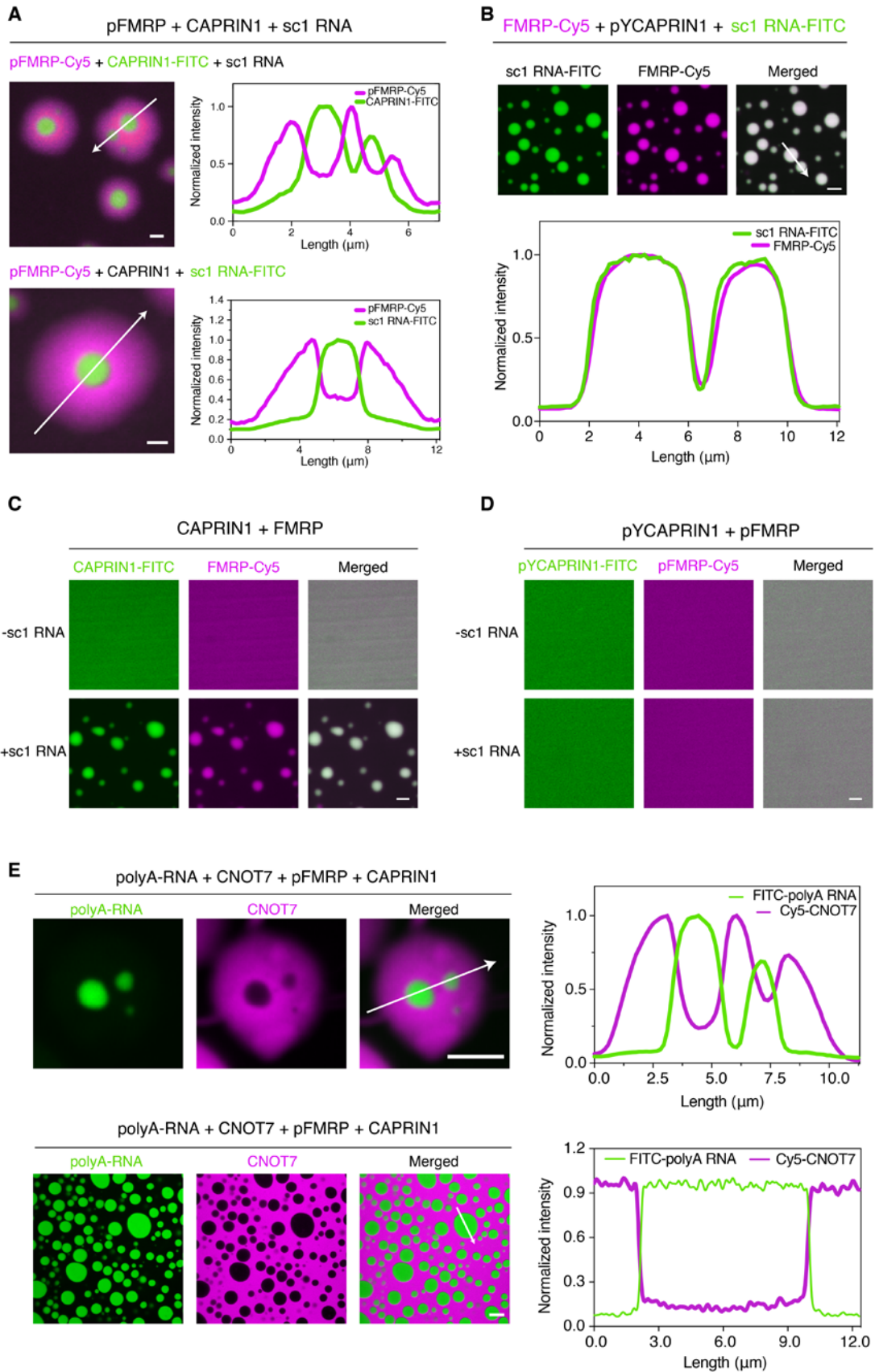


Fig. S12. pFMRP-CAPRIN1-sc1 RNA condensates form outer compartments enriched with pFMRP and inner compartments enriched with CAPRIN1 and sc1 RNA. (A) Cy5-labelled pFMRP and FITC-labelled CAPRIN1 are used for visualization of the proteins. (B) FITC-labelled sc1 RNA and Cy5-labelled pFMRP are used for visualization of the protein and RNA. (C, D) Droplets were observed when CAPRIN1 + FMRP was mixed with sc1 RNA. Droplets were absent in the case of CAPRIN1 + FMRP without sc1 RNA and pYCAPRIN1 + pFMRP with/without sc1 RNA. CAPRIN1 and FMRP concentrations are 100 μ M. pYCAPRIN1 and pFMRP concentrations are 30 μ M. sc1 RNA concentration is 3 μ M. Scale bars are 1.5 μ m. (E) Top, fluorescence images of polyA RNA-FITC and CNOT7-Cy5 in pFMRP and CAPRIN1 droplets were acquired with a spinning disk confocal microscope taken from Fig. 4B. Bottom, A higher resolution image with deconvolution processing. Intensity profiles between the two show sharper boundaries between polyA-RNA-FITC and CNOT7-Cy5. The image shows multiple CAPRIN1-RNA phases within an enlarged pFMRP-CNOT7 phase. Scale bars are 4.5 μ m.

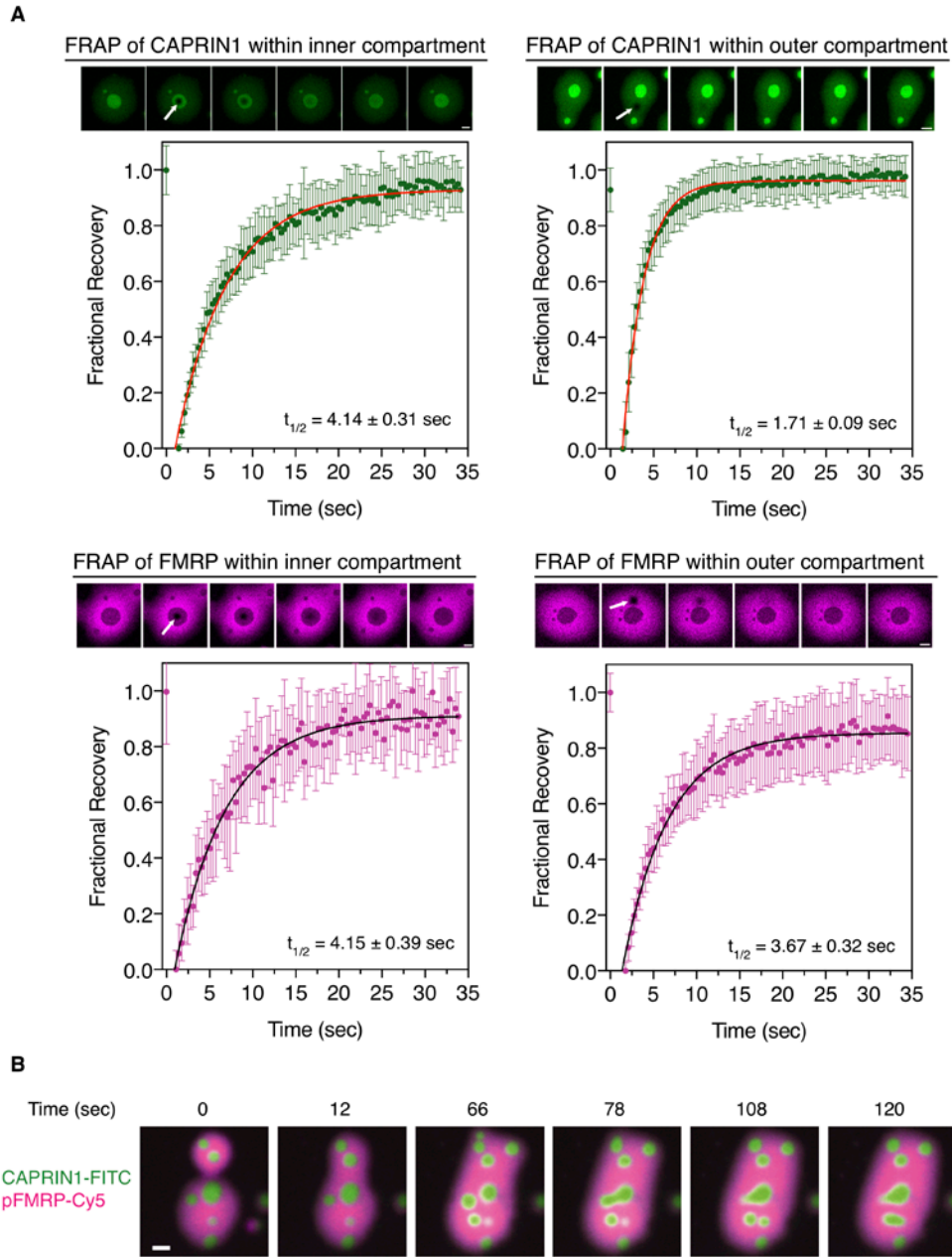


Fig. S13. Inner and outer compartments of pFMRP-CAPRIN1-RNA condensates are both dynamic and exhibit liquid properties. (A) Top. Fluorescence recovery after photobleaching (FRAP) experiments performed on CAPRIN1-FITC in the inner compartment (left) or CAPRIN1-FITC in the outer compartment (right). Bottom. FRAP experiments performed on pFMRP-Cy5 in the inner compartment (left) or pFMRP-Cy5 in the outer compartment (right). Nine FRAP profiles were averaged to obtain these profiles. Error bars represent standard deviations from 10 independent repeats. (B) Images from time-lapse fluorescence microscopy video showing fusion of inner and outer compartments, reflective of liquid properties. CAPRIN1 (or CAPRIN1-FITC) and pFMRP (or pFMRP-Cy5) concentrations are 100 and 30 μ M, respectively. sc1 RNA concentration is 3 μ M.

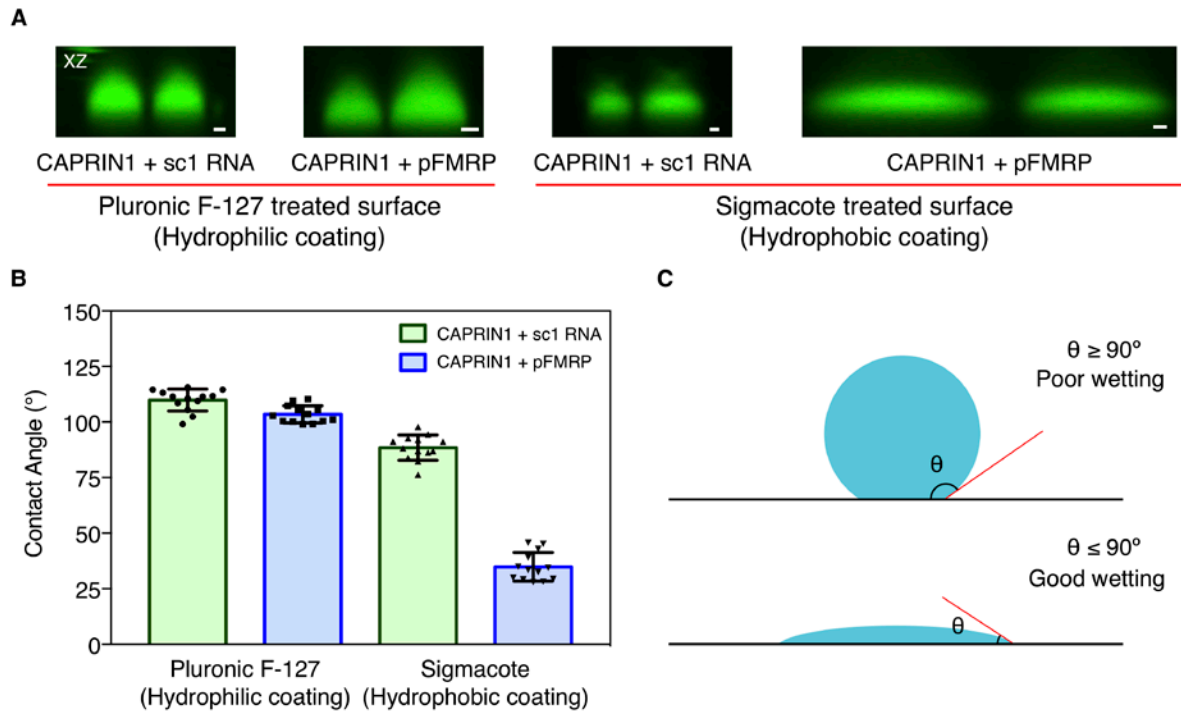


Fig. S14. Recapitulated separate compartments of the pFMRP-CAPRIN1-sc1 RNA multi-phase condensate show distinct biophysical properties determined by droplet wetting behaviour. (A) Fluorescence images of the recapitulated inner compartment represented by CAPRIN1-FITC and sc1 RNA and the recapitulated outer compartment represented by CAPRIN1-FITC and pFMRP placed on glass coverslips treated with a hydrophilic coating (Pluronic F-127) or hydrophobic coating (Sigmacote). CAPRIN1-FITC concentration is 100 μ M; pFMRP-Cy5 concentration is 30 μ M; and sc1 RNA concentration is 3 μ M. (B) Contact angles reflective of wetting properties were measured on each surface. Error bars represent standard deviation from 13 independent measurements in each coating. The recapitulated inner compartment has similar wetting behaviour in both hydrophilic ($110.0^\circ \pm 4.9^\circ$) and hydrophobic ($88.5^\circ \pm 5.7^\circ$) coating. The recapitulated outer compartment wets better on hydrophobic ($34.8^\circ \pm 6.4^\circ$) than hydrophilic ($103.4^\circ \pm 3.9^\circ$) coating. (C) A visual depiction of droplet wetting properties and contact angle measurements.

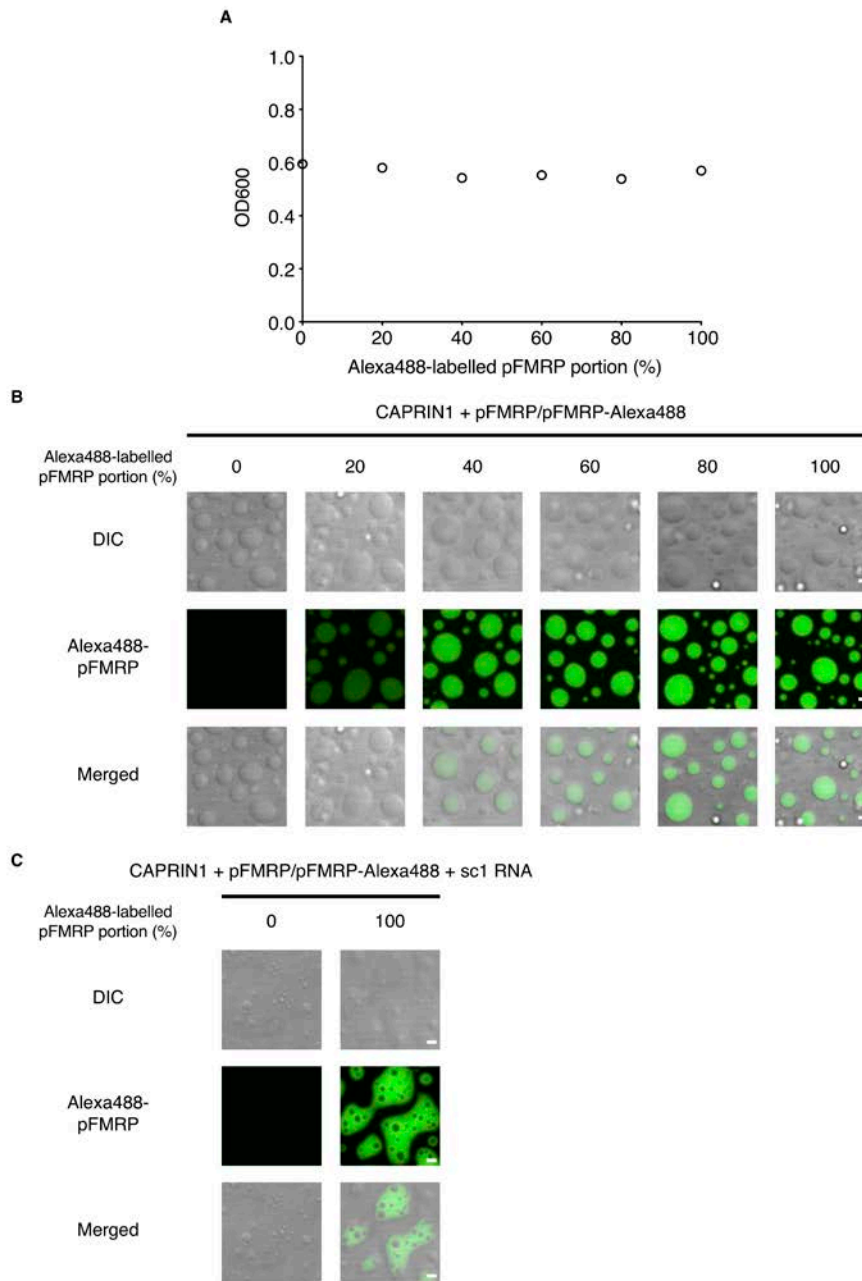


Fig. S15. Phase behaviour is not significantly affected by fluorophores. (A) Turbidity measurements (OD600) do not change significantly with an increasing amount of Alexa488-labelled pFMRP mixed with CAPRIN1. (B) Fluorescence microscope and differential interference contrast (DIC) images of the samples in (A) show the turbidities are due to droplet formations. Droplet morphologies do not change with an increasing amount of Alexa488-labelled pFMRP mixed with CAPRIN1. (C) DIC and fluorescence images of CAPRIN1 + pFMRP + sc1 RNA show sub-compartmentalization within droplets regardless of the presence of the Alexa488 fluorophore. Concentrations of CAPRIN1 and pFMRP (or pFMRP-Alexa488) are 200 and 30 μ M, respectively. sc1 RNA concentration is 3 μ M.

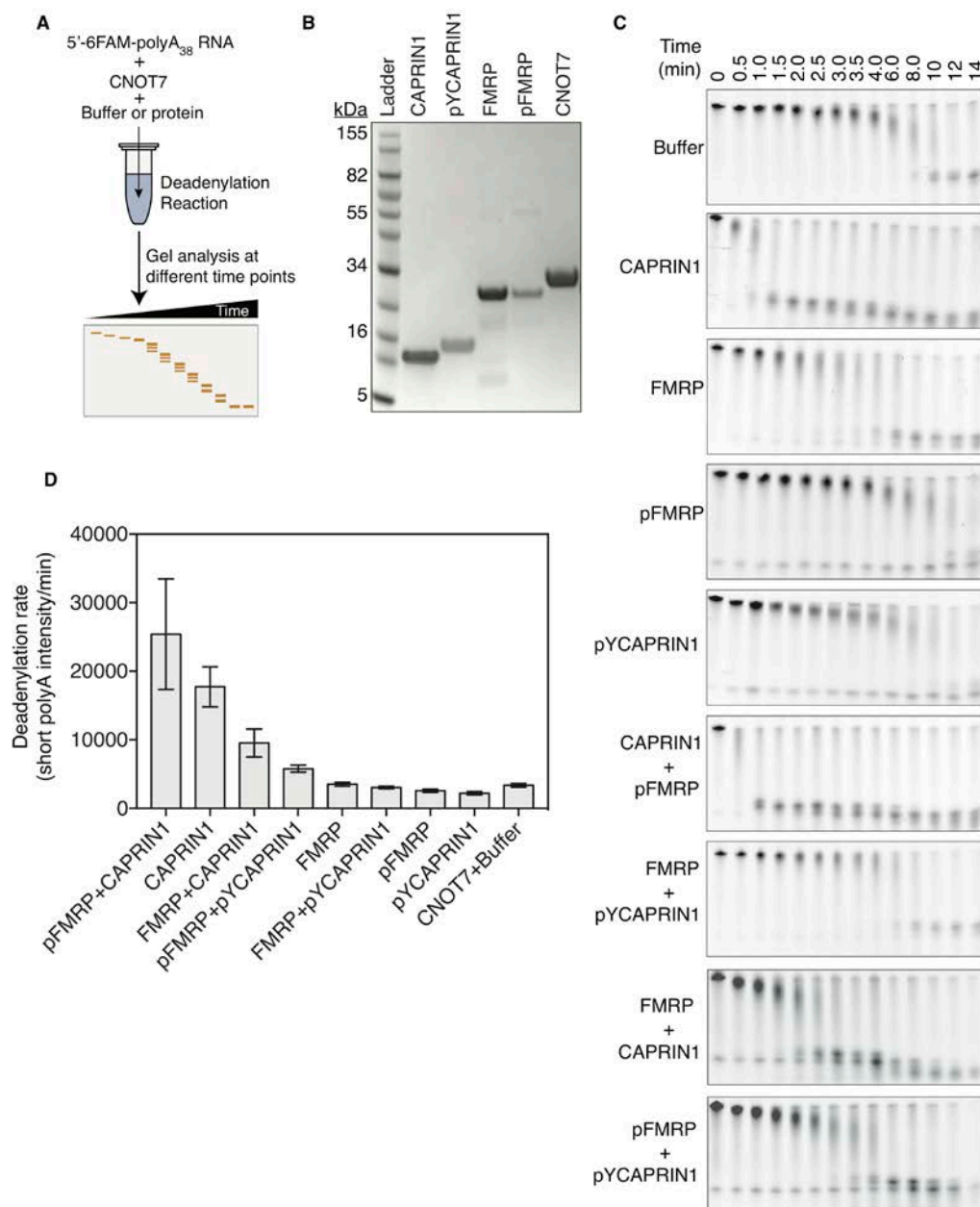


Fig. S16. Deadenylation activity monitored by gel-based assays that followed CNOT7 mediated cleavage of 5'-FITC-PolyA₃₈ RNA. (A) Schematic diagram of the deadenylation assay. (B) SDS-PAGE protein gel (stained with Coomassie blue) shows the purity of protein components used in the assay. (C) Representative deadenylation assay gels from mixing CNOT7 (5 μ M) and 5'-FITC-PolyA₃₈ RNA (50 nM) with specific protein components, CAPRIN1 (60 μ M), pYCAPRIN1 (60 μ M), FMRP (30 μ M), pFMRP (30 μ M). (D) Deadenylation rates were measured by densitometric intensities of the appearance of cleaved FITC-PolyA₃₈ RNA signal over time (min). Error bars are calculated based on the goodness of the fit (R^2).

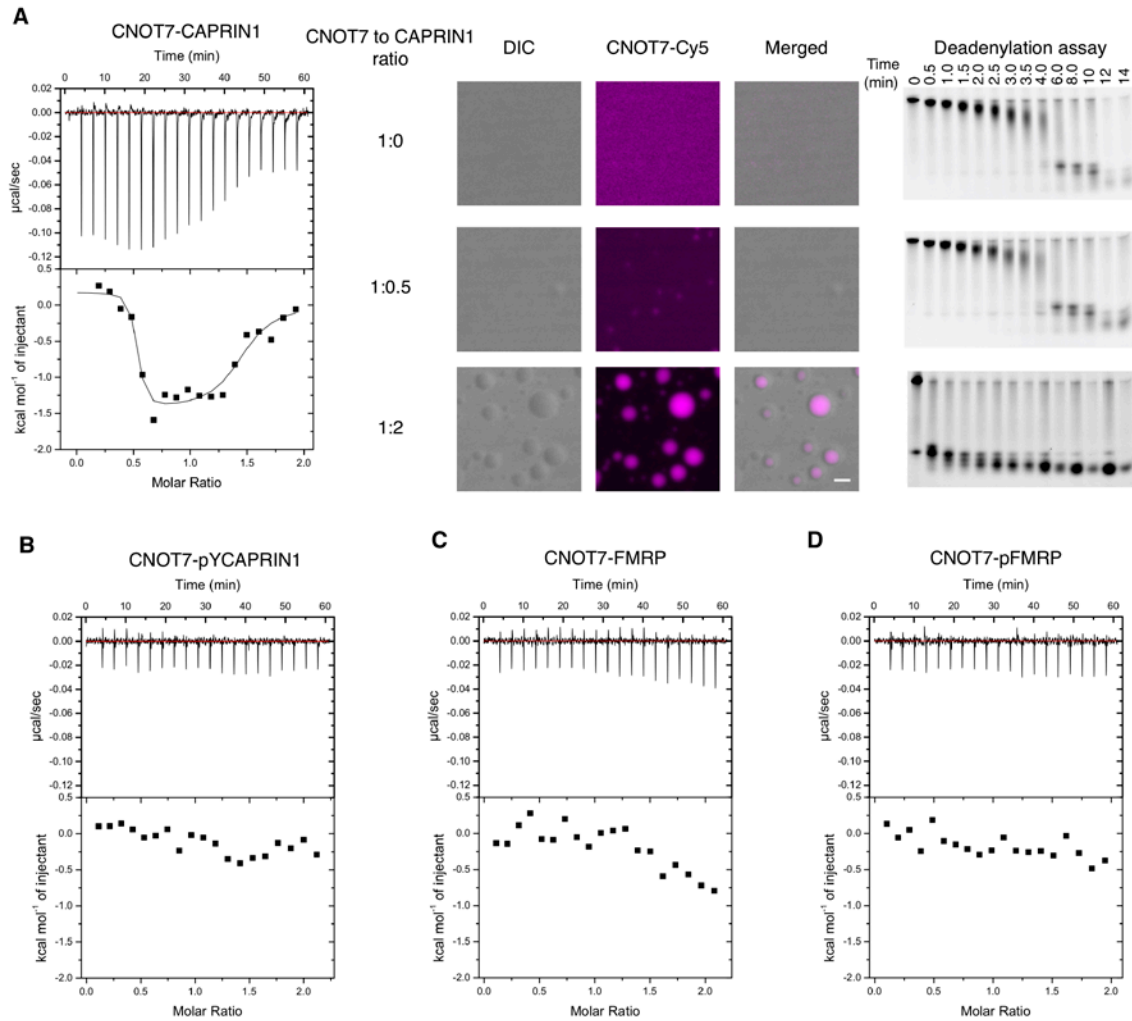


Fig. S17. CNOT7 interacts with CAPRIN1 in a biphasic manner due to binding and then phase separation, with only phase separation leading to enhanced activity, but does not interact significantly with pYCAPRIN1, FMRP, or pFMRP. (A) ITC curve of CAPRIN1 (100 µM) titrated into CNOT7 (10 µM) shows a biphasic interaction. Fluorescence images show the initial and latter changes in heat is due to the interaction of CNOT7 and CAPRIN1 in dilute phase and formation of droplets, respectively. Deadenylation assays of CNOT7 with varying amounts of CAPRIN1 show correlation between the enhancement of CNOT7 activity and droplet formations. (B) ITC curve of pYCAPRIN1 (100 µM) titrated into CNOT7 (10 µM). (C) ITC curve of FMRP (100 µM) titrated in CNOT7 (10 µM). (D) ITC curve of pFMRP (100 µM) titrated in CNOT7 (10 µM).

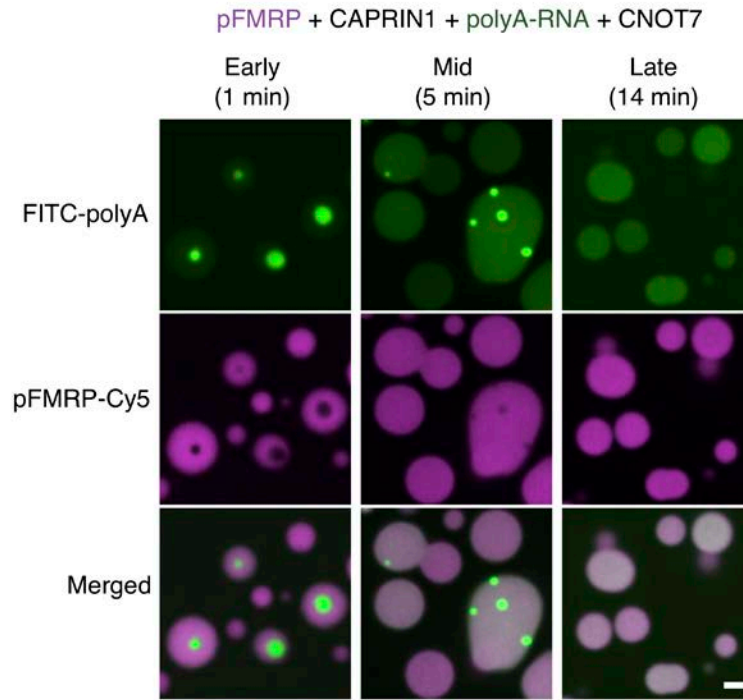


Fig. S18. Inner compartments of the multi-phase droplets of pFMRP-Cy5 + CAPRIN1 + polyA-RNA-FITC + CNOT7 shrink and disappear over time. Concentrations of pFMRP-Cy5, CAPRIN1, polyA-RNA-FITC, and CNOT7 were 30, 60, 1, and 5 μM , respectively. Scale bar is 2.1 μm .

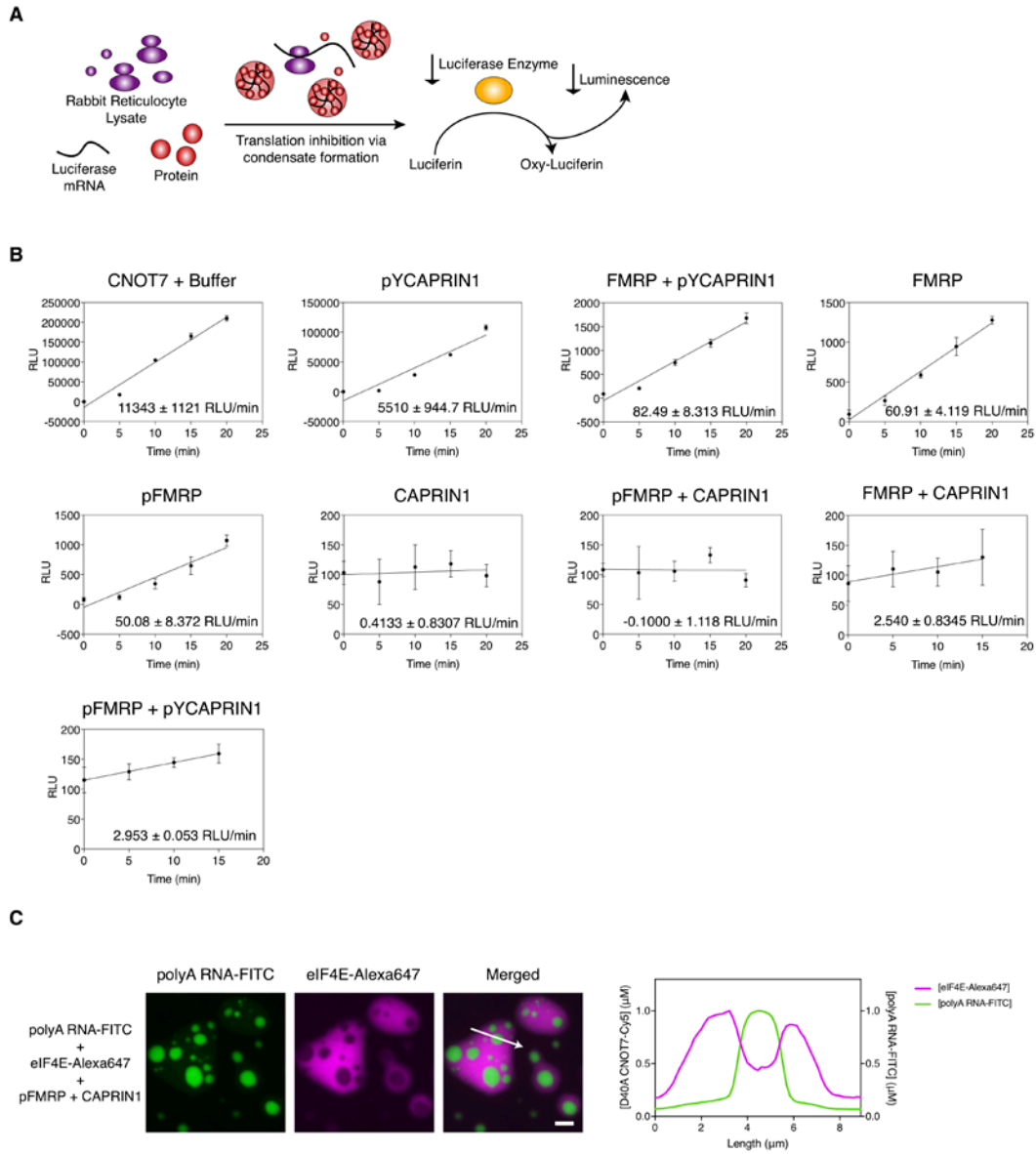


Fig. S19. *In vitro* translation rates are determined by luminescence activity as function of time. (A) Schematic diagram of translation assay with rabbit reticulocyte lysate and proteins. (B) Each individual plot represents the translation rates determined by the line of best fit of the relative luminescence units (RLU) as a function of time. Error bars represent standard deviation from a set of two independent experiments each measured three times. CNOT7 in buffer (11000 ± 1100 RLU/min) and pYCAPRIN1 (5500 ± 1000 RLU/min) exhibited the fastest translation rate while the translation was most inhibited in pFMRP-CAPRIN1 (-0.10 ± 1.12 RLU/min) and CAPRIN1 (0.41 ± 0.83 RLU/min). (C) Fluorescence images show predominant segregation of FITC labelled polyA RNA and Alexa647 labelled eIF4E, a critical component of the translational machinery. FITC-RNA and Alexa647-eIF4E were added to pre-formed pFMRP-CAPRIN1 droplets. Concentrations of polyA RNA-FITC, eIF4E-Alexa647, pFMRP and CAPRIN1 are 3, 10, 30 and 100 μM. Scale bar is 3 μm.

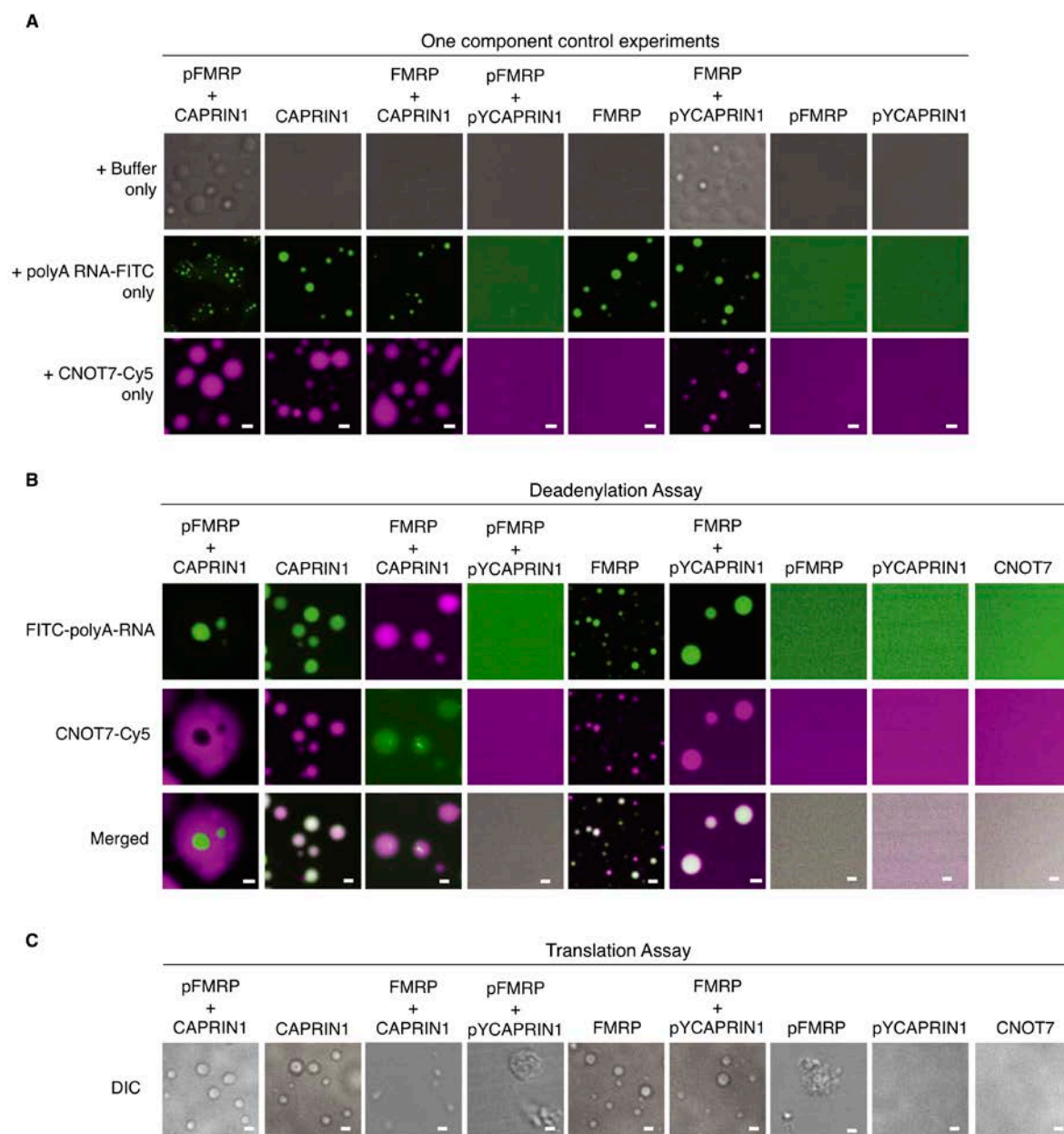


Fig. S20. Images of control, deadenylation and translation samples. (A) Fluorescence images and Differential interference contrast (DIC) of different combinations of FMRP and CAPRIN1 with/without phosphorylation were acquired in the presence of buffer, polyA RNA-FITC and CNOT7-Cy5. (B) FITC-labelled-polyA RNA and Cy5-labelled CNOT7 were used to examine formation of droplets in deadenylation assay samples. Droplets are observed in pFMRP+CAPRIN1, CAPRIN1, FMRP+CAPRIN1, FMRP, and FMRP+pYCAPRIN1 samples in the presence of CNOT7 and polyA RNA. No droplets were observed in pFMRP+CAPRIN1, pFMRP, pYCAPRIN1 and CNOT7 samples. Scale bars are 1.5 μ m. (C) DIC images show presence of droplets in pFMRP+CAPRIN1, CAPRIN1, FMRP+CAPRIN1, FMRP, FMRP+pYCAPRIN and CAPRIN1 translation assay samples. The pFMRP and

pFMRP+pYCAPRIN1 samples did not show simple droplet formation, potentially indicative of gelation or aggregation. No droplets were observed in pYCAPRIN1 and CNOT7 samples. Scale bars are 1.5 μm . CAPRIN1 (60 μM), pYCAPRIN1 (60 μM), FMRP (30 μM), pFMRP (30 μM) were used for deadenylation assays and control experiments. For translation experiments, 20 μM of proteins were used.

Movie S1. Time lapse movie of pFMRP-CAPRIN1-sc1 RNA.

Time lapse movie of pFMRP-CAPRIN1-sc1 RNA was recorded for 10 minutes. The liquid-like natures of both outer and inner compartments are apparent due to fusion. pFMRP (magenta) and CAPRIN1 (green) are labelled with Cy5 and FITC, respectively. Sc1-RNA is unlabeled.

CAPRIN1-FITC concentration is 100 μM ; pFMRP-Cy5 concentration is 30 μM ; and sc1 RNA concentration is 3 μM .

References

1. S. F. Banani, H. O. Lee, A. A. Hyman, M. K. Rosen, Biomolecular condensates: Organizers of cellular biochemistry. *Nat. Rev. Mol. Cell Biol.* **18**, 285–298 (2017).
[doi:10.1038/nrm.2017.7](https://doi.org/10.1038/nrm.2017.7) [Medline](#)
2. Y. Shin, C. P. Brangwynne, Liquid phase condensation in cell physiology and disease. *Science* **357**, eaaf4382 (2017). [doi:10.1126/science.aaf4382](https://doi.org/10.1126/science.aaf4382) [Medline](#)
3. K. Wiederhold, L. A. Passmore, Cytoplasmic deadenylation: Regulation of mRNA fate. *Biochem. Soc. Trans.* **38**, 1531–1536 (2010). [doi:10.1042/BST0381531](https://doi.org/10.1042/BST0381531) [Medline](#)
4. A. C. Goldstrohm, M. Wickens, Multifunctional deadenylase complexes diversify mRNA control. *Nat. Rev. Mol. Cell Biol.* **9**, 337–344 (2008). [doi:10.1038/nrm2370](https://doi.org/10.1038/nrm2370) [Medline](#)
5. M. W. Webster, Y.-H. Chen, J. A. W. Stowell, N. Alhusaini, T. Sweet, B. R. Graveley, J. Collier, L. A. Passmore, mRNA Deadenylation Is Coupled to Translation Rates by the Differential Activities of Ccr4-Not Nucleases. *Mol. Cell* **70**, 1089–1100.e8 (2018).
[doi:10.1016/j.molcel.2018.05.033](https://doi.org/10.1016/j.molcel.2018.05.033) [Medline](#)
6. J. R. Buchan, R. Parker, Eukaryotic stress granules: The ins and outs of translation. *Mol. Cell* **36**, 932–941 (2009). [doi:10.1016/j.molcel.2009.11.020](https://doi.org/10.1016/j.molcel.2009.11.020) [Medline](#)
7. A. M. Krichevsky, K. S. Kosik, Neuronal RNA granules: A link between RNA localization and stimulation-dependent translation. *Neuron* **32**, 683–696 (2001). [doi:10.1016/S0896-6273\(01\)00508-6](https://doi.org/10.1016/S0896-6273(01)00508-6) [Medline](#)
8. A. Hubstenberger, M. Courel, M. Bénard, S. Souquere, M. Ernoult-Lange, R. Chouaib, Z. Yi, J.-B. Morlot, A. Munier, M. Fradet, M. Daunesse, E. Bertrand, G. Pierron, J. Mozziconacci, M. Kress, D. Weil, P-Body Purification Reveals the Condensation of Repressed mRNA Regulons. *Mol. Cell* **68**, 144–157.e5 (2017).
[doi:10.1016/j.molcel.2017.09.003](https://doi.org/10.1016/j.molcel.2017.09.003) [Medline](#)
9. R. M. Vernon, P. A. Chong, B. Tsang, T. H. Kim, A. Bah, P. Farber, H. Lin, J. D. Forman-Kay, Pi-Pi contacts are an overlooked protein feature relevant to phase separation. *eLife* **7**, e31486 (2018). [doi:10.7554/eLife.31486](https://doi.org/10.7554/eLife.31486) [Medline](#)
10. J.-Y. Youn, W. H. Dunham, S. J. Hong, J. D. R. Knight, M. Bashkurov, G. I. Chen, H. Bagci, B. Rathod, G. MacLeod, S. W. M. Eng, S. Angers, Q. Morris, M. Fabian, J.-F. Côté, A.-C. Gingras, High-Density Proximity Mapping Reveals the Subcellular Organization of mRNA-Associated Granules and Bodies. *Mol. Cell* **69**, 517–532.e11 (2018).
[doi:10.1016/j.molcel.2017.12.020](https://doi.org/10.1016/j.molcel.2017.12.020) [Medline](#)
11. S. A. Barbee, P. S. Estes, A.-M. Cziko, J. Hillebrand, R. A. Luedeman, J. M. Collier, N. Johnson, I. C. Howlett, C. Geng, R. Ueda, A. H. Brand, S. F. Newbury, J. E. Wilhelm, R. B. Levine, A. Nakamura, R. Parker, M. Ramaswami, Staufen- and FMRP-containing

- neuronal RNPs are structurally and functionally related to somatic P bodies. *Neuron* **52**, 997–1009 (2006). [doi:10.1016/j.neuron.2006.10.028](https://doi.org/10.1016/j.neuron.2006.10.028) [Medline](#)
12. R. El Fatimy, S. Tremblay, A. Y. Dury, S. Solomon, P. De Koninck, J. W. Schrader, E. W. Khandjian, Fragile X mental retardation protein interacts with the RNA-binding protein Caprin1 in neuronal RiboNucleoProtein complexes. *PLOS ONE* **7**, e39338 (2012). [doi:10.1371/journal.pone.0039338](https://doi.org/10.1371/journal.pone.0039338) [Medline](#)
 13. S. De Rubeis, C. Bagni, Fragile X mental retardation protein control of neuronal mRNA metabolism: Insights into mRNA stability. *Mol. Cell. Neurosci.* **43**, 43–50 (2010). [doi:10.1016/j.mcn.2009.09.013](https://doi.org/10.1016/j.mcn.2009.09.013) [Medline](#)
 14. D.-I. Kao, G. M. Aldridge, I. J. Weiler, W. T. Greenough, Altered mRNA transport, docking, and protein translation in neurons lacking fragile X mental retardation protein. *Proc. Natl. Acad. Sci. U.S.A.* **107**, 15601–15606 (2010). [doi:10.1073/pnas.1010564107](https://doi.org/10.1073/pnas.1010564107) [Medline](#)
 15. S. Solomon, Y. Xu, B. Wang, M. D. David, P. Schubert, D. Kennedy, J. W. Schrader, Distinct structural features of caprin-1 mediate its interaction with G3BP-1 and its induction of phosphorylation of eukaryotic translation initiation factor 2alpha, entry to cytoplasmic stress granules, and selective interaction with a subset of mRNAs. *Mol. Cell. Biol.* **27**, 2324–2342 (2007). [doi:10.1128/MCB.02300-06](https://doi.org/10.1128/MCB.02300-06) [Medline](#)
 16. M. A. Kiebler, G. J. Bassell, Neuronal RNA granules: Movers and makers. *Neuron* **51**, 685–690 (2006). [doi:10.1016/j.neuron.2006.08.021](https://doi.org/10.1016/j.neuron.2006.08.021) [Medline](#)
 17. K. Nakayama, R. Ohashi, Y. Shinoda, M. Yamazaki, M. Abe, A. Fujikawa, S. Shigenobu, A. Futatsugi, M. Noda, K. Mikoshiba, T. Furuichi, K. Sakimura, N. Shiina, RNG105/caprin1, an RNA granule protein for dendritic mRNA localization, is essential for long-term memory formation. *eLife* **6**, e29677 (2017). [doi:10.7554/eLife.29677](https://doi.org/10.7554/eLife.29677) [Medline](#)
 18. B. Tsang, J. Arsenault, R. M. Vernon, H. Lin, N. Sonenberg, L.-Y. Wang, A. Bah, J. D. Forman-Kay, Phosphoregulated FMRP phase separation models activity-dependent translation through bidirectional control of mRNA granule formation. *Proc. Natl. Acad. Sci. U.S.A.* **116**, 4218–4227 (2019). [doi:10.1073/pnas.1814385116](https://doi.org/10.1073/pnas.1814385116) [Medline](#)
 19. J. Sheu-Gruttadauria, I. J. MacRae, Phase Transitions in the Assembly and Function of Human miRISC. *Cell* **173**, 946–957.e16 (2018). [doi:10.1016/j.cell.2018.02.051](https://doi.org/10.1016/j.cell.2018.02.051) [Medline](#)
 20. X. Su, J. A. Ditlev, E. Hui, W. Xing, S. Banjade, J. Okrut, D. S. King, J. Taunton, M. K. Rosen, R. D. Vale, Phase separation of signaling molecules promotes T cell receptor signal transduction. *Science* **352**, 595–599 (2016). [doi:10.1126/science.aad9964](https://doi.org/10.1126/science.aad9964) [Medline](#)
 21. E. R. Towers, J. J. Kelly, R. Sud, J. E. Gale, S. J. Dawson, Caprin-1 is a target of the deafness gene Pou4f3 and is recruited to stress granules in cochlear hair cells in response to ototoxic damage. *J. Cell Sci.* **124**, 1145–1155 (2011). [doi:10.1242/jcs.076141](https://doi.org/10.1242/jcs.076141) [Medline](#)

22. P. V. Hornbeck, B. Zhang, B. Murray, J. M. Kornhauser, V. Latham, E. Skrzypek, PhosphoSitePlus, 2014: Mutations, PTMs and recalibrations. *Nucleic Acids Res.* **43**, D512–D520 (2015). [doi:10.1093/nar/gku1267](https://doi.org/10.1093/nar/gku1267) [Medline](#)
23. M. C. Siomi, K. Higashijima, A. Ishizuka, H. Siomi, Casein kinase II phosphorylates the fragile X mental retardation protein and modulates its biological properties. *Mol. Cell. Biol.* **22**, 8438–8447 (2002). [doi:10.1128/MCB.22.24.8438-8447.2002](https://doi.org/10.1128/MCB.22.24.8438-8447.2002) [Medline](#)
24. K. A. Burke, A. M. Janke, C. L. Rhine, N. L. Fawzi, Residue-by-Residue View of In Vitro FUS Granules that Bind the C-Terminal Domain of RNA Polymerase II. *Mol. Cell* **60**, 231–241 (2015). [doi:10.1016/j.molcel.2015.09.006](https://doi.org/10.1016/j.molcel.2015.09.006) [Medline](#)
25. J. P. Brady, P. J. Farber, A. Sekhar, Y.-H. Lin, R. Huang, A. Bah, T. J. Nott, H. S. Chan, A. J. Baldwin, J. D. Forman-Kay, L. E. Kay, Structural and hydrodynamic properties of an intrinsically disordered region of a germ cell-specific protein on phase separation. *Proc. Natl. Acad. Sci. U.S.A.* **114**, E8194–E8203 (2017). [doi:10.1073/pnas.1706197114](https://doi.org/10.1073/pnas.1706197114) [Medline](#)
26. T. J. Nott, E. Petsalaki, P. Farber, D. Jarvis, E. Fussner, A. Plochowitz, T. D. Craggs, D. P. Bazett-Jones, T. Pawson, J. D. Forman-Kay, A. J. Baldwin, Phase transition of a disordered nuage protein generates environmentally responsive membraneless organelles. *Mol. Cell* **57**, 936–947 (2015). [doi:10.1016/j.molcel.2015.01.013](https://doi.org/10.1016/j.molcel.2015.01.013) [Medline](#)
27. A. T. Phan, V. Kuryavyi, J. C. Darnell, A. Serganov, A. Majumdar, S. Ilin, T. Raslin, A. Polonskaia, C. Chen, D. Clain, R. B. Darnell, D. J. Patel, Structure-function studies of FMRP RGG peptide recognition of an RNA duplex-quadruplex junction. *Nat. Struct. Mol. Biol.* **18**, 796–804 (2011). [doi:10.1038/nsmb.2064](https://doi.org/10.1038/nsmb.2064) [Medline](#)
28. M. Feric, N. Vaidya, T. S. Harmon, D. M. Mitrea, L. Zhu, T. M. Richardson, R. W. Kriwacki, R. V. Pappu, C. P. Brangwynne, Coexisting Liquid Phases Underlie Nucleolar Subcompartments. *Cell* **165**, 1686–1697 (2016). [doi:10.1016/j.cell.2016.04.047](https://doi.org/10.1016/j.cell.2016.04.047) [Medline](#)
29. R. L. McFleder, F. Mansur, J. D. Richter, Dynamic Control of Dendritic mRNA Expression by CNOT7 Regulates Synaptic Efficacy and Higher Cognitive Function. *Cell Rep.* **20**, 683–696 (2017). [doi:10.1016/j.celrep.2017.06.078](https://doi.org/10.1016/j.celrep.2017.06.078) [Medline](#)
30. J. Pelletier, N. Sonenberg, The Organizing Principles of Eukaryotic Ribosome Recruitment. *Annu. Rev. Biochem.* **88**, 307–335 (2019). [doi:10.1146/annurev-biochem-013118-111042](https://doi.org/10.1146/annurev-biochem-013118-111042) [Medline](#)
31. S. Wiesner, L. E. Wybenga-Groot, N. Warner, H. Lin, T. Pawson, J. D. Forman-Kay, F. Sicheri, A change in conformational dynamics underlies the activation of Eph receptor tyrosine kinases. *EMBO J.* **25**, 4686–4696 (2006). [doi:10.1038/sj.emboj.7601315](https://doi.org/10.1038/sj.emboj.7601315) [Medline](#)
32. M. Sattler, J. Schleucher, C. Griesinger, Heteronuclear multidimensional NMR experiments for the structure determination of proteins in solution employing pulsed field gradients.

- Prog. Nucl. Magn. Reson. Spectrosc.* **34**, 93–158 (1999). [doi:10.1016/S0079-6565\(98\)00025-9](https://doi.org/10.1016/S0079-6565(98)00025-9)
33. W. Bermel, I. Bertini, I. C. Felli, R. Kümmerle, R. Pierattelli, Novel ^{13}C direct detection experiments, including extension to the third dimension, to perform the complete assignment of proteins. *J. Magn. Reson.* **178**, 56–64 (2006). [doi:10.1016/j.jmr.2005.08.011](https://doi.org/10.1016/j.jmr.2005.08.011) [Medline](#)
34. W. Bermel, I. Bertini, I. C. Felli, M. Piccioli, R. Pierattelli, ^{13}C -detected protonless NMR spectroscopy of proteins in solution. *Prog. Nucl. Magn. Reson. Spectrosc.* **48**, 25–45 (2006). [doi:10.1016/j.pnmrs.2005.09.002](https://doi.org/10.1016/j.pnmrs.2005.09.002)
35. F. Delaglio, S. Grzesiek, G. W. Vuister, G. Zhu, J. Pfeifer, A. Bax, NMRPipe: A multidimensional spectral processing system based on UNIX pipes. *J. Biomol. NMR* **6**, 277–293 (1995). [doi:10.1007/BF00197809](https://doi.org/10.1007/BF00197809) [Medline](#)
36. W. F. Vranken, W. Boucher, T. J. Stevens, R. H. Fogh, A. Pajon, M. Llinas, E. L. Ulrich, J. L. Markley, J. Ionides, E. D. Laue, The CCPN data model for NMR spectroscopy: Development of a software pipeline. *Proteins* **59**, 687–696 (2005). [doi:10.1002/prot.20449](https://doi.org/10.1002/prot.20449) [Medline](#)
37. H. Mi, X. Huang, A. Muruganujan, H. Tang, C. Mills, D. Kang, P. D. Thomas, PANTHER version 11: Expanded annotation data from Gene Ontology and Reactome pathways, and data analysis tool enhancements. *Nucleic Acids Res.* **45**, D183–D189 (2017). [doi:10.1093/nar/gkw1138](https://doi.org/10.1093/nar/gkw1138) [Medline](#)
38. S. De Rubeis, C. Bagni, Regulation of molecular pathways in the Fragile X Syndrome: Insights into Autism Spectrum Disorders. *J. Neurodev. Disord.* **3**, 257–269 (2011). [doi:10.1007/s11689-011-9087-2](https://doi.org/10.1007/s11689-011-9087-2) [Medline](#)
39. Y. Wu, J. Zhu, X. Huang, Z. Du, Crystal structure of a dimerization domain of human Caprin-1: Insights into the assembly of an evolutionarily conserved ribonucleoprotein complex consisting of Caprin-1, FMRP and G3BP1. *Acta Crystallogr. D* **72**, 718–727 (2016). [doi:10.1107/S2059798316004903](https://doi.org/10.1107/S2059798316004903) [Medline](#)
40. J. Kim, J. Daniel, A. Espejo, A. Lake, M. Krishna, L. Xia, Y. Zhang, M. T. Bedford, Tudor, MBT and chromo domains gauge the degree of lysine methylation. *EMBO Rep.* **7**, 397–403 (2006). [Medline](#)
41. J. Côté, S. Richard, Tudor domains bind symmetrical dimethylated arginines. *J. Biol. Chem.* **280**, 28476–28483 (2005). [doi:10.1074/jbc.M414328200](https://doi.org/10.1074/jbc.M414328200) [Medline](#)
42. A. Ramos, D. Hollingworth, A. Pastore, G-quartet-dependent recognition between the FMRP RGG box and RNA. *RNA* **9**, 1198–1207 (2003). [doi:10.1261/rna.5960503](https://doi.org/10.1261/rna.5960503) [Medline](#)

43. Y.-T. Shirai, T. Suzuki, M. Morita, A. Takahashi, T. Yamamoto, Multifunctional roles of the mammalian CCR4-NOT complex in physiological phenomena. *Front. Genet.* **5**, 286 (2014). [doi:10.3389/fgene.2014.00286](https://doi.org/10.3389/fgene.2014.00286) [Medline](#)
44. M. R. Fabian, F. Frank, C. Rouya, N. Siddiqui, W. S. Lai, A. Karetnikov, P. J. Blackshear, B. Nagar, N. Sonenberg, Structural basis for the recruitment of the human CCR4-NOT deadenylase complex by tristetraprolin. *Nat. Struct. Mol. Biol.* **20**, 735–739 (2013). [doi:10.1038/nsmb.2572](https://doi.org/10.1038/nsmb.2572) [Medline](#)
45. V. Tugarinov, R. Muhandiram, A. Ayed, L. E. Kay, Four-dimensional NMR spectroscopy of a 723-residue protein: Chemical shift assignments and secondary structure of malate synthase G. *J. Am. Chem. Soc.* **124**, 10025–10035 (2002). [doi:10.1021/ja0205636](https://doi.org/10.1021/ja0205636) [Medline](#)
46. J. A. Ditlev, L. B. Case, M. K. Rosen, Who's In and Who's Out-Compositional Control of Biomolecular Condensates. *J. Mol. Biol.* **430**, 4666–4684 (2018). [doi:10.1016/j.jmb.2018.08.003](https://doi.org/10.1016/j.jmb.2018.08.003) [Medline](#)
47. Z. Bozoky, M. Krzeminski, R. Muhandiram, J. R. Birtley, A. Al-Zahrani, P. J. Thomas, R. A. Frizzell, R. C. Ford, J. D. Forman-Kay, Regulatory R region of the CFTR chloride channel is a dynamic integrator of phospho-dependent intra- and intermolecular interactions. *Proc. Natl. Acad. Sci. U.S.A.* **110**, E4427–E4436 (2013). [doi:10.1073/pnas.1315104110](https://doi.org/10.1073/pnas.1315104110) [Medline](#)
48. I. N. Shatsky, I. M. Terenin, V. V. Smirnova, D. E. Andreev, Cap-Independent Translation: What's in a Name? *Trends Biochem. Sci.* **43**, 882–895 (2018). [doi:10.1016/j.tibs.2018.04.011](https://doi.org/10.1016/j.tibs.2018.04.011) [Medline](#)
49. B. C. Avanzino, G. Fuchs, C. S. Fraser, Cellular cap-binding protein, eIF4E, promotes picornavirus genome restructuring and translation. *Proc. Natl. Acad. Sci. U.S.A.* **114**, 9611–9616 (2017). [doi:10.1073/pnas.1704390114](https://doi.org/10.1073/pnas.1704390114) [Medline](#)
50. N. Kedersha, M. D. Panas, C. A. Achorn, S. Lyons, S. Tisdale, T. Hickman, M. Thomas, J. Lieberman, G. M. McInerney, P. Ivanov, P. Anderson, G3BP-Caprin1-USP10 complexes mediate stress granule condensation and associate with 40S subunits. *J. Cell Biol.* **212**, 845–860 (2016). [doi:10.1083/jcb.201508028](https://doi.org/10.1083/jcb.201508028) [Medline](#)
51. K. Peng, P. Radivojac, S. Vucetic, A. K. Dunker, Z. Obradovic, Length-dependent prediction of protein intrinsic disorder. *BMC Bioinformatics* **7**, 208 (2006). [doi:10.1186/1471-2105-7-208](https://doi.org/10.1186/1471-2105-7-208) [Medline](#)
52. F. Meggio, L. A. Pinna, One-thousand-and-one substrates of protein kinase CK2? *FASEB J.* **17**, 349–368 (2003). [doi:10.1096/fj.02-0473rev](https://doi.org/10.1096/fj.02-0473rev) [Medline](#)